JGR Solid Earth

RESEARCH ARTICLE
10.1029/2024JB029001

Mechanical Stiffness and Permeability of a Reservoir-Scale Rough Fracture During Closure

Qinglin Deng[1,2], Jean Schmittbuhl[2], Mauro Cacace[3], and Guido Blöcher[3,4]

[1]State Key Laboratory of Coal Mine Disaster Dynamics and Control, School of Resources and Safety Engineering, Chongqing University, Chongqing, China, [2]EOST/ITES, Université de Strasbourg/CNRS, Strasbourg, France, [3]GFZ German Research Centre for Geosciences, Potsdam, Germany, [4]Department of Engineering Geology, TU Berlin, Berlin, Germany

Key Points:

- A hydro-mechanical numerical model of the closure of a rough fracture at field scale is built using observed multi-scale fracture geometry
- The largely observed stiffness characteristic is shown to be related to the self-affine property of the fracture surface
- The increase of fracture stiffness with decreasing fracture permeability is shown to be exponential up to the percolation threshold

Supporting Information:

Supporting Information may be found in the online version of this article.

Correspondence to:

J. Schmittbuhl,
jean.schmittbuhl@unistra.fr

Citation:

Deng, Q., Schmittbuhl, J., Cacace, M., & Blöcher, G. (2024). Mechanical stiffness and permeability of a reservoir-scale rough fracture during closure. *Journal of Geophysical Research: Solid Earth*, *129*, e2024JB029001. https://doi.org/10.1029/2024JB029001

Received 28 FEB 2024
Accepted 2 SEP 2024

Author Contributions:

Conceptualization: Qinglin Deng, Jean Schmittbuhl, Guido Blöcher
Data curation: Qinglin Deng, Guido Blöcher
Formal analysis: Qinglin Deng, Jean Schmittbuhl, Mauro Cacace, Guido Blöcher
Funding acquisition: Jean Schmittbuhl, Guido Blöcher
Investigation: Jean Schmittbuhl, Guido Blöcher
Methodology: Qinglin Deng, Jean Schmittbuhl, Mauro Cacace, Guido Blöcher

Abstract

We study how the normal stiffness and the permeability of a realistic rough fracture at the field scale are linked and evolve during its closure up to the percolation threshold. We base our approach on a well-established self-affine geometric model for fracture roughness, which has proven to be a relevant proxy from laboratory to multi-kilometer scales. We explore its implications for fracture apertures in reservoir-scale open channels. We build our approach on a finite element model using the MOOSE/GOLEM framework and conduct numerical flow-through experiments in a $256 \times 256 \times 256$ m^3 granite reservoir hosting a single, partially sealed fracture under variable normal loading conditions and undrained conditions. Navier-Stokes flow is solved in the embedded 3-dimensional rough fracture, and Darcy flow is solved in the surrounding poroelastic matrix. We study the evolution of the mechanical stiffness and fluid permeability of the fracture-rock system during fracture closure including mechanisms that impact the contact surface geometry like asperity yield and deposit of fracture-filling material in the open space of the rough fracture. The largely observed stiffness characteristic is shown to be related to the self-affine property of the fracture surface. A strong anisotropy of the fracture permeability is evidenced when the fluid percolation thresholds are exceeded in two orthogonal directions of the imposed pressure gradient. We propose a unifying physically based law for the evolution of stiffness and permeability in the form of an exponential increase in stiffness as permeability decreases.

Plain Language Summary

Natural or artificial fluid flow in deep fractured reservoirs, such as enhanced geothermal systems (EGS), is primarily controlled by open fractures and faults, and is considered a key element for hydraulic performance. On the one hand, flow along these fractures is strongly affected by channeling between fracture asperities and fracture sealing along the open fracture space. On the other hand, fracture asperities and fracture seals also impact the mechanical behavior of fractures, especially their mechanical stiffness. Here, we study how the stiffness and the permeability of a realistic rough fracture at the field scale are linked and evolve during its closure. We show that the mechanical stiffness is exponentially increasing when the fracture permeability is decreasing. Moreover, this stiffness-permeability law is unique both during the mechanical and the chemical closure, being strongly related to the effective contact area along the fracture. The results have implications for large scale assessment of hydraulic properties of fractures and fractured reservoir stimulation.

1. Introduction

Fractures play a major role as preferential fluid pathways for numerous georesource applications, such as deep geothermal reservoirs (Cox, 2005; Gudmundsson, 2011; Huenges & Ledru, 2011; R. W. Zimmerman & Bodvarsson, 1996). Indeed, they provide major conduits at all scales through which fluids can flow (Berkowitz, 2002; Caine et al., 1996). They are also critical for the mechanical behavior of fractured rock masses owing to their ubiquity and the fact that they are typically mechanically weak objects (R. Zimmerman & Main, 2004). Subsequently, the hydromechanical behavior of rock fractures is of central importance for determining the transport and deformation properties of faulted reservoirs. This behavior can be studied for the fractured rock mass that includes fracture networks with many fractures but also for a single fracture (Adler & Thovert, 1999; Cornet, 2015; De Dreuzy et al., 2012; Deng et al., 2021; Kluge et al., 2020; Scholz, 2019). Indeed, the behavior of a single fracture must be addressed first to understand that of the whole fractured mass. Although numerous studies have addressed the behavior of a single fracture at laboratory scales (1 cm–1 m), much less describe its behavior at field scale (10–1,000 m).

Project administration: Jean Schmittbuhl, Guido Blöcher
Resources: Jean Schmittbuhl, Guido Blöcher
Software: Qinglin Deng, Mauro Cacace, Guido Blöcher
Supervision: Jean Schmittbuhl, Mauro Cacace, Guido Blöcher
Validation: Qinglin Deng, Jean Schmittbuhl, Mauro Cacace, Guido Blöcher
Visualization: Qinglin Deng, Mauro Cacace, Guido Blöcher
Writing – original draft: Qinglin Deng, Jean Schmittbuhl
Writing – review & editing: Qinglin Deng, Jean Schmittbuhl, Mauro Cacace, Guido Blöcher

As demonstrated by numerous studies, the fundamental properties of individual fractures strongly rely on the geometry of the fracture void space and the contact area between the facing fracture walls (Barton & Choubey, 1977; Gudmundsson, 2011; Jaeger et al., 2009; Kluge, Blöcher, et al., 2021; Scholz, 2019). Fracture roughness, which controls the fracture void space geometry, has been extensively analyzed in the past by using various techniques to measure the fracture surface topography (Bouchaud, 1997; Brown & Scholz, 1985; Power & Tullis, 1991; Schmittbuhl, Schmitt, & Scholz, 1995; Tse & Cruden, 1979). Among the techniques that characterize the fracture and fault roughness from topography measurements (Candela et al., 2009; Schmittbuhl, Vilotte, & Roux, 1995), spectral analysis is more generally used to demonstrate the power law behavior of the height-height correlation function (Jacobs et al., 2017). It is shown that the fracture surfaces of different rock materials, with different fracture modes and within different geological contexts share a self-affine scaling invariance that extends up to a multi-kilometric fault scale with no roll-off wavelength at large scales (Candela et al., 2012; Fardin et al., 2001; Sagy et al., 2007; Schmittbuhl, Gentier, & Roux, 1993). In some cases, the self-affine geometrical model of the fault surface exhibits anisotropy related to the main slip direction with anisotropy in the Hurst or roughness exponent (Brodsky et al., 2011; Candela et al., 2012; Renard et al., 2006).

As a fracture is mechanically loaded, its contact area is expected to increase, and a percolation threshold for fluid flow might be reached (Dapp et al., 2012; Sahimi, 1993; Schmittbuhl, Vilotte, & Roux, 1993). The contact mechanics of self-affine surfaces have been explored by numerous studies (Almqvist et al., 2011; Batrouni et al., 2002; Borri-Brunetto et al., 1999; Carbone & Bottiglione, 2008; Hyun et al., 2004; Pastewka et al., 2013; Pei et al., 2005; Persson, 2006; Persson et al., 2004; Vallet et al., 2009). They show specific properties such as (a) a linear relationship between the contact area and normal loading; (b) an exponential evolution of the normal stress with respect to the normal displacement; and (c) a linear increase in the normal fracture stiffness with normal stress. These studies have also shown that the normal stress field along asperities exhibits self-affine properties (Hansen et al., 2000; Schmittbuhl et al., 2006). Experimental measurements of the fracture stiffness have also been obtained from laboratory mechanical tests (Evans et al., 1992; L. J. Pyrak-Nolte et al., 1990; Zangerl et al., 2008; L. J. Pyrak-Nolte, 2019; Zhou et al., 2020). They show that stress effect on the stiffness could be consistent with that of a self-affine model of the fracture topography but also some departures from the linear relationship.

Natural sealing might also impact the closure of a fracture (P. S. Lang et al., 2016). Sealing derives from many processes and is dependent on the fluid chemistry, temperature, and pressure (Parry, 1998). Following the pioneering work of Durney (1973), the following three fracture filling modes are defined: the syntaxial mode for inward growth, antitaxial mode for outward growth, and stretching mode for an unspecific growth direction. The growth of seals in deforming rocks can arise from a single event, but it is often the result of multiple crack sealing events following fracture growth (Bons et al., 2012). Then, the fibrous habits of crystalline materials induced by pressure solution in the rock matrix are shown (Laubach, 2003; Ramsay, 1980). Dissolution and precipitation along fracture walls owing to secondary mineral deposition or artificial reactive fluid injection might also significantly modify the permeability and stiffness of fractures (Laubach, 2003; Liu et al., 2006; Elkhoury et al., 2013; Noiriel et al., 2013; P. Lang et al., 2015). Changes in stiffness from sealing bridge development along fractures can have large-scale implications by inducing, for instance, seismic velocity variations (Sayers et al., 2009).

When fractures close, their permeability is expected to change significantly. Permeability of rough fractures is typically studied using single-phase fluid flow in the open void space of the rough fractures, particularly in the framework of the lubrication approximation, where the roughness is considered as a perturbation to a parallel plate model (R. W. Zimmerman & Bodvarsson, 1996). The cubic law is then applied to relate the mechanical aperture of the fracture, that is, the average of the geometrical aperture, to the fracture permeability. Another approach is to define the hydraulic aperture of a fracture based on its hydraulic properties. Numerous models and experiments have been developed to compare the mechanical and hydraulic apertures of fractures for different flow regimes (Mourzenko et al., 1995; R. W. Zimmerman & Bodvarsson, 1996; Méheust & Schmittbuhl, 2000, 2001; Matsuki et al., 2006; Ishibashi et al., 2015; Kluge et al., 2017; Huang et al., 2019). These works demonstrate the impact of the fracture roughness on the fracture permeability with regard to the enhancement or inhibition of the flow owing to strong channeling of the flow for a specific orientation of the pressure drop. Shear history of the fracture has also a strong impact on the anisotropy of the permeability (P. S. Lang et al., 2018). Moreover, the largest wavelengths in the aperture field are shown to dominate the influence of the roughness (Neuville et al., 2010a; Neuville et al., 2010b; M. Wang et al., 2016). In the case of many independent fractures, fracture

roughness is shown, on average, to inhibit flow when a hydraulic aperture is smaller than the mechanical aperture as the fracture surfaces come into contact. However, significant departures from this average behavior exist since the behavior is dominated by the largest wavelengths, which are not stationary in space and are accordingly specific to each surface.

Our study aims to assess the relative evolution of the normal stiffness and the permeability of a fracture during its closure, a topic with important implications for geo-engineering (Li et al., 2021). One specific contribution of our approach is to develop our model at the reservoir scale (100–1,000 m), using multi-scale knowledge of fracture geometry, and combining the mechanical effect of asperity yield and the chemical effect of mineral deposit, two mechanisms that are expected to dominantly impact the fracture contact area. For the mechanical effect, we simplify the contact rheology, and assume that the deformation of asperities follows a rigid-plastic behavior (i.e., rigid solid with a low yield stress) since normal stresses strongly concentrate on a limited set of contact points where the elastic limit is exceeded. We show that this approach is a good proxy of a full elasto-plastic model. We also compare our approach to the well-known empirical law of stiffness evolution from Bandis et al. (1983). For the description of the sealing process, we simplify the details of the sealing mineral deposition to a progressive filling of the aperture by a set of discrete homogeneous layers. Minerals are supposed to be typically elongated in the growth direction perpendicular to the fracture walls, forming homogeneous layers in which the thickness is controlled by precipitation kinetics and the fracture opening rate (Bons et al., 2012; Ramsay, 1980). Successive layers then fill the open space of the fracture and modify the permeability and stiffness of the fracture. Their effects on the fracture stiffness result from the competition between the progressive evolution of the contact area owing to the mechanical closure of the fracture filling with competent cement and the generation of new bridges between the fracture walls in the asperities neighborhood. The evolution of the fault open volume, fracture normal stiffness, and permeability are analyzed until fluid percolation thresholds are exceeded in two orthogonal directions of the imposed pressure gradient where a strong anisotropy of the fracture permeability is evidenced. We propose a unifying physically based law for the evolution of stiffness and permeability in the form of an exponential increase in stiffness as permeability decreases. Finally, we discuss the hydraulic and geomechanical implications of the stiffness-permeability evolution for reservoirs.

2. Model Description

2.1. Fluid Flow in a Partially Open Fracture Embedded in a Porous Rock Under Normal Load

Figure 1 shows the model geometry with a large-scale partially open fracture embedded in a 3D poro-elastic block. The dimensions of the entire block are $256 \times 256 \times 256 \mathrm{m}^3$, which represent a characteristic scale of a typical fractured/faulted reservoir, for example, the Soultz-Sous-Forêts deep geothermal reservoir (Vallier et al., 2019). The fracture is partially open due to the presence of fracture asperities that define open domains where fluid can flow. We assume drained conditions, that is, fluid is able to move along the fracture due to an imposed pressure difference at the boundaries. Fluid circulation is modeled by imposing a pressure gradient (constant pressures at the inlet and outlet boundaries) along either the x-direction or y-direction of the block to investigate a possible anisotropy in the fluid flow behavior. The contact areas between asperities are the domains where stress is transferred with no fluid flow, that is, closed domains. We assume that the fracture is mechanically loaded by a normal stress σ_n applied along the top of the block. Because of the partial contact along the fracture, the applied stress on the whole block boundary is amplified along the contact zones following Amonton's law, as shown in Figure 1a (Scholz, 2019). Figure 1b shows an example of the fluid flow both in the pores of the matrix and in the open space of the fracture for a case when the pressure gradient is imposed along the x-direction.

2.2. Fracture Aperture

Faults and fractures are typically considered two-dimensional objects. This is because their thicknesses are often considered negligible with respect to their extension. They are then approximated as planar surfaces. However, even as 2D objects, they show multiscale corrugations that can be described by a self-affine topography over a large range of scales (up to 9 decades of length scales) (Candela et al., 2012). A 2D cross-section of the fault will then remain statistically invariant under the following scaling transformation: $\delta x \rightarrow \lambda \delta x$, $\delta z \rightarrow \lambda^H \delta z$, where δx is the coordinate along the section, δz is the topography amplitude and H is the Hurst or roughness exponent (Meakin, 1998; Schmittbuhl, Schmitt, & Scholz, 1995). Moreover (Candela et al., 2012; Renard et al., 2006), showed that faults/fractures exhibit a certain anisotropy in their roughness exponent in response to the fault slip

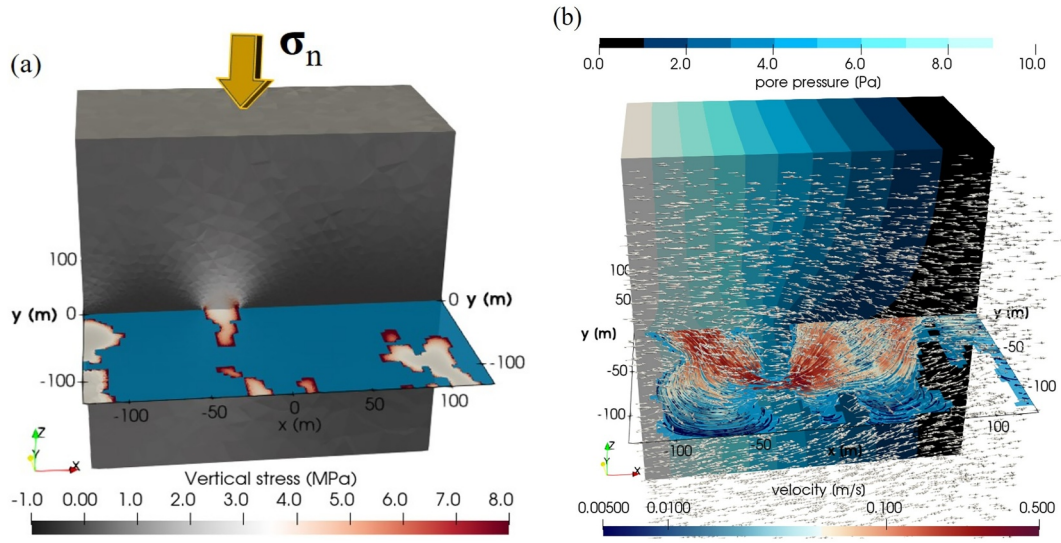

Figure 1. Sketch of the model: a partially open fault (colored horizontal cross-section) is embedded in a 3D block (in dark gray) of size $256 \times 256 \times 256\text{m}^3$ loaded by a normal stress σ_n. (a) The contact areas (in light gray) along the fracture support the applied normal stress with variable local amplification of the stress (reddish zones). The open part of the fracture where fluid circulates is shown in blue. (b) 3D view of the fluid circulation in the fracture (colored horizontal cross-section) and in the pore space of the matrix (white arrows) when a pressure drop is applied in the x-direction (the vertical thick, blue layers indicate the pressure field in the matrix). The contact areas are transparent here.

history, resulting in a roughness exponent on the order of $H_{\parallel} = 0.6$ along the slip direction and $H_{\perp} = 0.8$ in the slip perpendicular direction.

Here, we consider a 256 m × 256 m three-dimensional fault with distributed aperture that reproduces the geometry of a natural fault at typical reservoir scales. The spectral properties of the synthetic fault geometry are consistent with those of a natural fault (Candela et al., 2012). We assume that the time scale of fluid flow is much shorter than that of the long-term shear slip along the fault, which is responsible for the anisotropy in the fault geometry. The fault geometry is then considered fixed during the flow simulation. Based on the fault topography, we build the fault aperture with the following assumption regarding the fault slip history: the cumulative fault shear offset is supposed to be large compared to the size of the fault area we are considering (Plouraboué et al., 1995). In this case, correlations between the two facing surfaces are lost, and the fault aperture is composed of the facing of two independent fault surfaces and subsequently has the same scaling properties of each fracture surface.

To reproduce field observations, we generate the fault aperture as an anisotropic self-affine surface with $H_{\parallel} = 0.6$ along the historical slip direction (y-axis) of the fault, $H_{\perp} = 0.8$ along the perpendicular direction (x-axis) and an RMS amplitude of 0.09 m for the fault topography at the scale of 256 m (see Figure 2a) (Candela et al., 2012). Figure 2b shows the histogram of the aperture distribution in the entire fault domain of 256 m × 256 m with no normal deformation of the asperities or no filling material in the openings of the fault. The measured distribution is well approximated by a Gaussian distribution. It is of interest to note that such a fault model predicts a typical magnitude for fault asperities on the order of 0.09 m for a fault with an extension of 256 m. The aspect ratio of such a 3D fault geometry is then on the order of $0.09\text{ m}/256\text{ m} \approx 3 \cdot 10^{-4}$. We also see that the maximal amplitude of the asperities is on the order of $3h_{rms} \approx 0.27$ m. In the (unrealistic) case of a fully rigid matrix, that is, no deformation of the largest asperities, this would correspond to the typical aperture of the fracture. As discussed below, the aperture will actually decrease when considering elasto-plastic deformation of the asperities under normal mechanical loading of the fault. The aperture is also expected to decrease when healing processes develop over time.

To explore the variability of the fracture geometry, six independent synthetic fractures are generated: F1, F2, F3, F4, F5, and F6 (See Supporting Information S1). They all share the same self-affine scaling properties, that is, the same roughness exponents and roughness amplitude at the same scale. The only difference among them is that

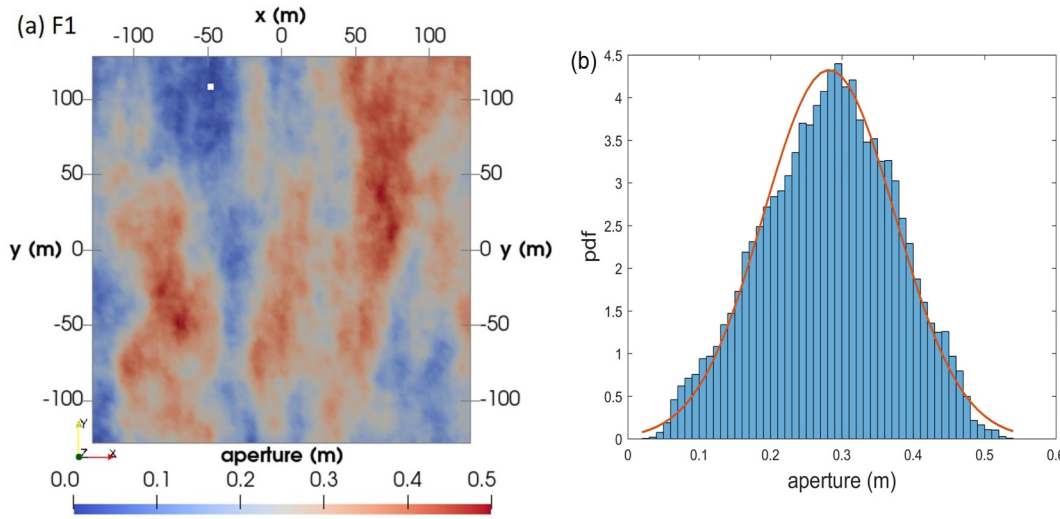

Figure 2. Generation of the fracture topology and aperture map: (a) Aperture map with only a few contact points; (b) power density function (PDF) of the aperture distribution with a Gaussian fit (bin width is 1 cm; average aperture is $\bar{h} = 0.27$ m; RMS is $h_{rms} = 0.09$ m).

different seeds are selected for generating the initial white noise signal, which is used to construct the self-affine fracture surface (Candela et al., 2009). As such, the six fractures have different surface or aperture geometries but still share the same statistical properties regarding their distribution. By way of illustration, the aperture map of F1 prior to any mechanical loading or sealing is shown in Figure 2a.

2.3. A Kinematic Model for Reconstructing the Fracture Closure

In this study, we assess both the mechanical and hydraulic properties of a fracture by modeling its closure following a specific conceptual route. Indeed, we reconstruct the closure of the fracture assuming that it is the result of two different mechanisms sequentially (Figure 3).

First, we consider that the fracture is only mechanically closed due to an increase in normal displacement applied along the top of block u_b from normal loading σ_n (see Figure 4). No sealing process is considered during this phase. The matrix and the fracture are shown as strings in series for which the bulk displacement u_b is the sum of the displacement of the matrix u_m and that of the fracture u_f. In other words, the fracture displacement u_f is equivalent to the difference between the vertical displacement of the fractured rock u_b and the intact rock matrix u_m, as follows:

$$u_f = u_b - u_m \tag{1}$$

Note that in this paper, the direction along negative z is considered positive. Therefore, the fracture closure u_f is positive with respect to the zero displacement of the first contact.

To simplify the contact rheology, we assume that the deformation of asperities follows a rigid-plastic behavior (i.e., rigid solid with a low yield stress). The normal loading then creates contact areas where stresses strongly concentrate and rapidly overpass the elastic limit, leading to a perfectly plastic behavior (Pei et al., 2005). This is similar to an "overlap" model where overlapping asperities are erased with volume losses (Figure 3c) (Kim et al., 2003; Méheust & Schmittbuhl, 2003; Walsh et al., 2008). As shown below and in Supporting Information S1 (Figures S3, S4 (Figure S4a) and S5), this approach is a relevant proxy of a full elasto-plastic model. This approximation minimizes contact areas since contact regions develop mainly along the highest asperities in compacted clustered regions and the deformation is local without volume conservation. In contrast, in a fully elastic model, contact areas would spread out over multiple regions because of non-local deformation and the additional requirement of volume preservation. Our choice of an "overlap" model stems from this model being supported by laboratory observations where deformation in contact/overlap areas produces gouge particles that are flowing out of the contact areas (Kluge, Bruhn, et al., 2021). The initial mechanical load leads to rigid plastic

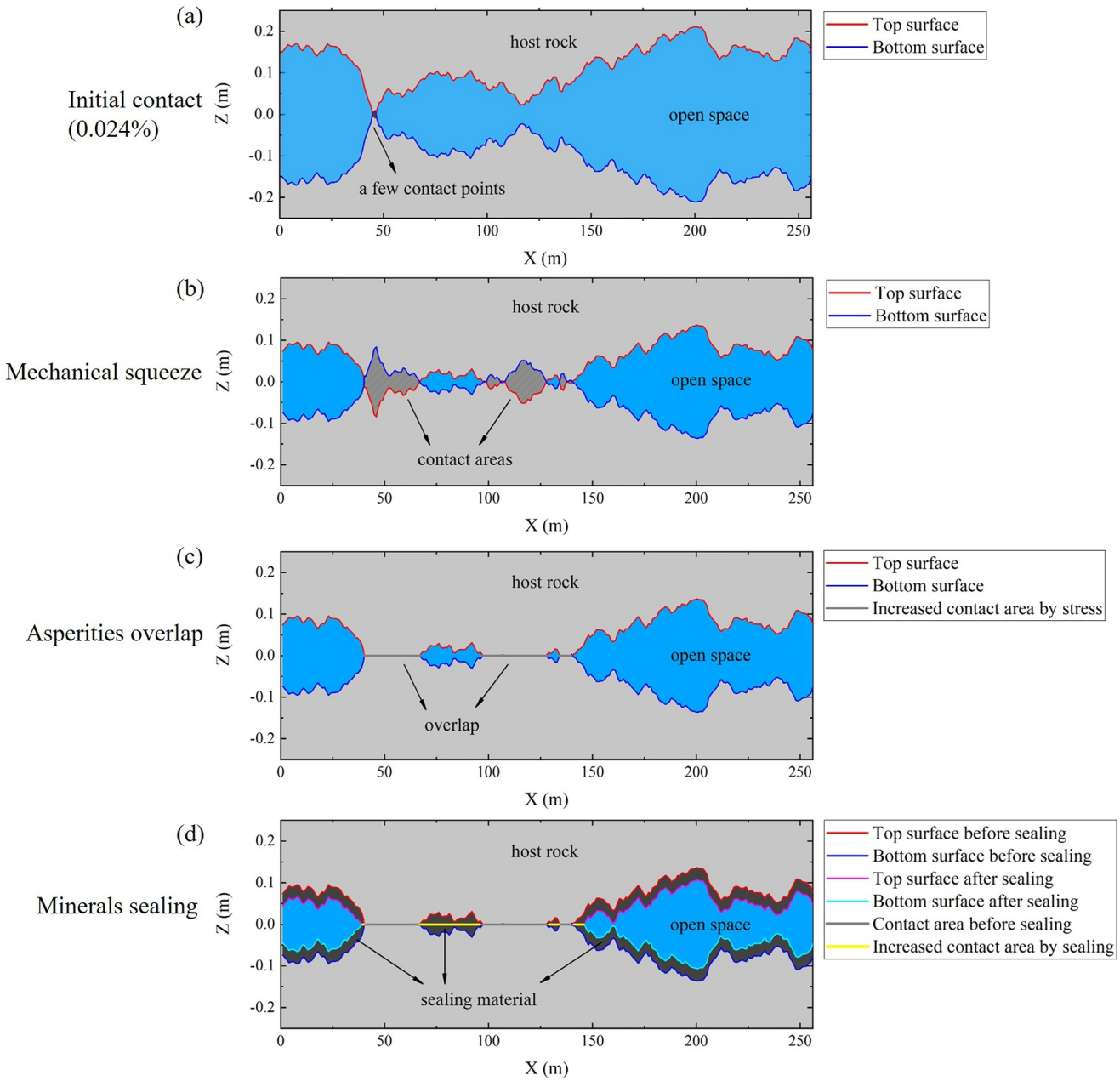

Figure 3. Cross-section through the block along the *x*-direction with a large vertical magnification to show the fracture closure process due to two different mechanisms. (a) Initial unloaded fracture aperture: fracture surfaces are just touching one another at a few contact points. (b) Phase 1—mechanical closure (contact area < 20%): the contact area increases because of a normal loading (imposed normal displacement) applied on the top of the host rock; (c) asperities that overlap following a "rigid-plastic" behavior. (d) Phase 2—sealing closure due to mineral deposits (contact area > 20%). Successive layers of sealing material are assumed to grow homogeneously with a constant thickness from the border to the center of the open space (syntaxial mode). The open space for fluid flow is shown in light blue, whereas the host rock is shown in light gray.

deformation and accumulation of elastic strain, and a stress release would lead to an elastic relaxation as indicated by the dashed red lines on the *x*-axis (Kluge, Bruhn, et al., 2021); in this case, plastic deformation will remain. We consider mechanical closure to be part of the initial history of the fracture, and it occurs before sealing begins to be effective. We assume that this phase leads to an overall contact area on the order of 20%, as observed in fracture closure experiments for a normal load on the order of several tens of MPa (Kluge, Bruhn, et al., 2021). During this mechanical phase of closure, the normal stress along the contact areas increases as the fracture displacement rises, leading to a more significant closure of the fracture, as shown in Figure 5.

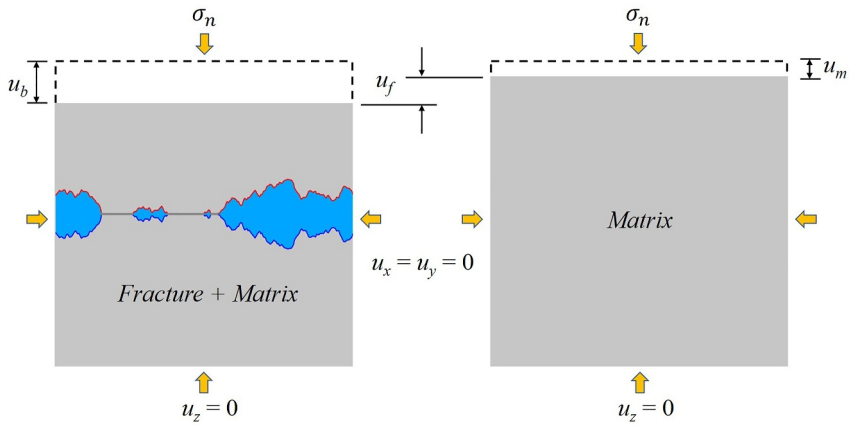

Figure 4. Definition of the fracture displacement: $u_f = u_b - u_m$, where u_b is the displacement of the fracture-matrix system, while u_m is the displacement of the intact rock matrix under the same applied normal loading σ_n.

The second mechanism for fracture closure is supposed to be due to a sealing process that occurs in the later stage, upon termination of the mechanical phase (i.e., typically when the contact area > 20%) at constant imposed normal displacement and normal stress (Figures 3c and 5). Fracture sealing is considered to be the sole result of mineral precipitation of successive layers, as commonly observed in fractured reservoirs (e.g., Griffiths et al., 2016). Homogeneous layers of secondary minerals are observed to be deposited with a rather constant thickness, following a syntaxial growth of the filling material, both in the field (Davis et al., 2011; Durney, 1973) and in laboratory hydrothermal experiments (Okamoto & Sekine, 2011). Specifically, during syntaxial growth, filling materials are progressively added from the fracture walls to the open space as opposed to during antitaxial growth, where the filling materials are added from the open space to the walls (Davis et al., 2011). Sealing would increase the stiffness of the system, as indicated by the extended dashed line in Figure 5. Therefore, the system could sustain more stress without additional plastic deformation. This will also lead to a transformation into a more elastic regime.

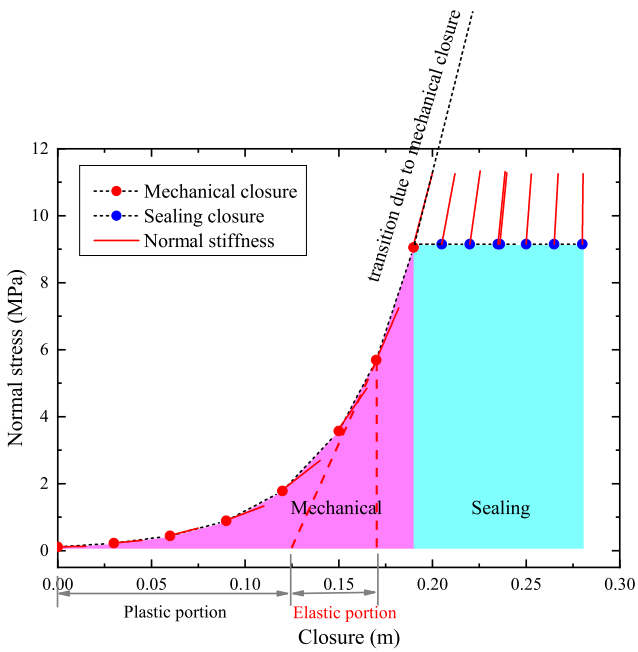

Figure 5. Evolution of the normal stress over the fracture closure (imposed displacement). The slopes of the red lines at each step of the mechanical/sealing closure correspond to the normal stiffness.

It is then of interest to note that this second part of the closure modeling can also be viewed as an "overlap" model since asperities are also erased due to a different physical mechanism, namely, during chemical sealing, the contact areas are expanding because of the outer growth of the asperity boundaries, while during mechanical closure, plastic deformation induces the inner movement of the asperity boundaries. Subsequently, we expect that in both cases, the stiffness and permeability of the fracture will be impacted in a similar manner and, thus, that they can be described by a common generic law. The whole fracture closure process can then be viewed as a progressive, continuous translation of one surface toward the other from the first contact points when the closure is zero to the full contact when the closure is at its maximum. This corresponds to a kinetic description of the aperture geometry evolution caused by steps of imposed displacements of one facing fracture penetrating the other. During the mechanical phase, the closure is equal to the relative imposed displacement u_f from its value at the first contact. During the sealing phase, the closure steps correspond to the thickness of the deposited layer. By gradually closing a fracture using this kinematic model, the relative contact area $y = A_c/A$ is shown to follow an error function law, that is, $y = (1 + erf(x/\sqrt{2}))/2$, as a function of the normalized closure $x = (u_f - \bar{h})/h_{rms}$, where u_f is the closure, $\bar{h}$ is the mechanical aperture of the initial fracture and h_{rms} its RMS. This law describes the cumulative distribution function (CDF) of a normal distribution (see the orange line in Figure 6). The pink area shows the mechanical closure (below 20% of the

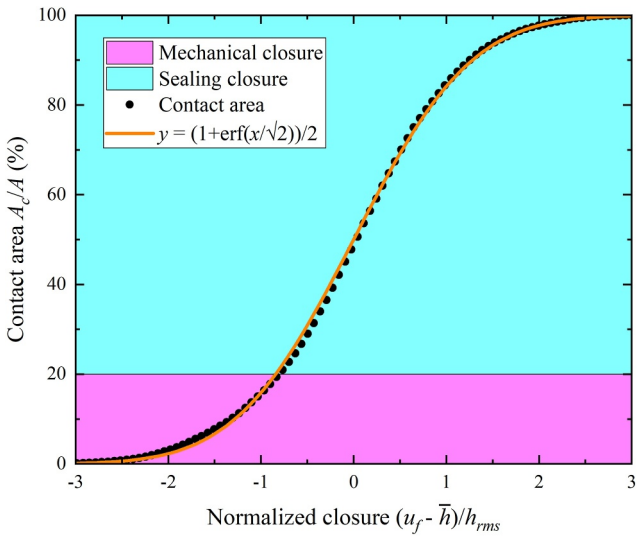

Figure 6. Evolution of the relative contact area A_c/A as a function of the normalized normal displacement imposed on the fractured block $(u_f - \bar{h})/h_{rms}$, where the mean aperture is $\bar{h}$ and the RMS is h_{rms}. The pink domain corresponds to the mechanical closure of the fracture, assuming an overlapping model of contact (i.e., purely plastic rheology of the asperities). The light blue domain corresponds to the sealing closure due to homogeneous mineral deposits in the open fracture space. The evolution of the contact area can be fitted by the cumulative distribution function of a normal distribution $y = (1 + erf(x/\sqrt{2}))/2$. The transition from a mechanical to a sealing closure is defined at 20% of contact, which corresponds to $(u_f - \bar{h})/h_{rms} \sim -1$.

contact area), while the light blue area shows the sealing closure (above 20% of the contact area).

2.4. Numerical Method

Analyzing the stress, pressure, and velocity fields in the fracture-matrix system requires an adequate physical model of the processes involved and their coupling. Here, the Multiphysics Object Oriented Simulation Environment (MOOSE) in combination with GOLEM, a MOOSE-based application for modeling coupled thermal-hydraulic-mechanical (THM) processes in fractured and faulted geothermal reservoirs, is used (Cacace & Jacquey, 2017; Jacquey et al., 2017; Peterson et al., 2018). We based our approach on separating two domains under undrained conditions (Figure 8): the porous matrix where fluid flow is driven by Darcy's equation and the fracture domain where Navier-Stokes equation is solved considering variations in the fracture volume due to the fracture closure process. Porosity changes in the model are supposed to be dominated by the fracture porosity changes described in Section 2.3 and matrix porosity is considered constant. Therefore, poro-elastic coupling in our model is related to changes of the fracture open space and not to that of the porous rock matrix.

Under these approximation, the mass conservation in the matrix leads to:

$$\frac{1}{M_b}\frac{\partial p_f}{\partial t} + \nabla \cdot \boldsymbol{q_D} + \boldsymbol{q_D} \cdot \frac{1}{K_f}\nabla p_f + \boldsymbol{v_s} \cdot \left(\frac{1}{M_b}\nabla p_f - \frac{1}{K_s}\nabla \cdot \left(\boldsymbol{\sigma} - \alpha p_f \boldsymbol{I}\right)\right) = 0 \quad (2)$$

where p_f is the pressure of the fluid, $\frac{1}{M_b} = \frac{\phi}{K_f} + \frac{\alpha - \phi}{K_s}$ is the specific storage of the matrix, K_f, the fluid bulk modulus, K_s, the bulk modulus of the solid grains, α, the Biot coefficient, ϕ, the porosity, $\boldsymbol{q_D}$, the volumetric flow rate per unit surface area, $\boldsymbol{v_s}$, the solid velocity, and $\boldsymbol{\sigma}$, the effective stress (assuming compressive positive pore pressure). The moment balance equation is expressed as:

$$\nabla \cdot \left(\boldsymbol{\sigma} - \alpha p_f \boldsymbol{I}\right) + \rho_b \boldsymbol{g} = 0 \quad (3)$$

where ρ_b is the bulk density $\left(\rho_b = \phi\rho_f + (1-\phi)\rho_s\right)$, ρ_f, the fluid density, ρ_s, the solid density, and $\boldsymbol{g}$ the gravity vector. For the fluid phase in the matrix, we assume a Darcy's flow, as follows:

$$\boldsymbol{q}_D = \phi\left(\boldsymbol{v_f} - \boldsymbol{v_s}\right) = -\frac{\boldsymbol{k_m}}{\mu_f} \cdot \left(\nabla p_f - \rho_f \boldsymbol{g}\right) \quad (4)$$

where $\boldsymbol{v_f}$, the fluid velocity, $\boldsymbol{k_m}$, the permeability tensor of the rock matrix, and μ_f, the dynamic fluid viscosity.

For the fluid phase in the open space of the fracture, the incompressible Navier-Stokes (INS) equation is implemented as follows for each step of the fracture closure (Peterson et al., 2018):

$$\rho_f \frac{D^f \boldsymbol{v_f}}{Dt} + \nabla p_f - \mu_f \nabla^2 \boldsymbol{v_f} - \rho_f \boldsymbol{g} = 0 \quad (5)$$

where D^f/Dt is the Lagrangian derivative with respect to the moving fluid. The use of INS for the fluid flow in the open space is motivated by the fact that we are searching for steady state solutions, the fracture closure being much slower than the fluid pressure diffusion.

The system of equations is spatially discretized by the finite element method, while temporal discretization relies on a finite difference implicit Euler scheme (Cacace & Jacquey, 2017). A generic workflow of the numerical

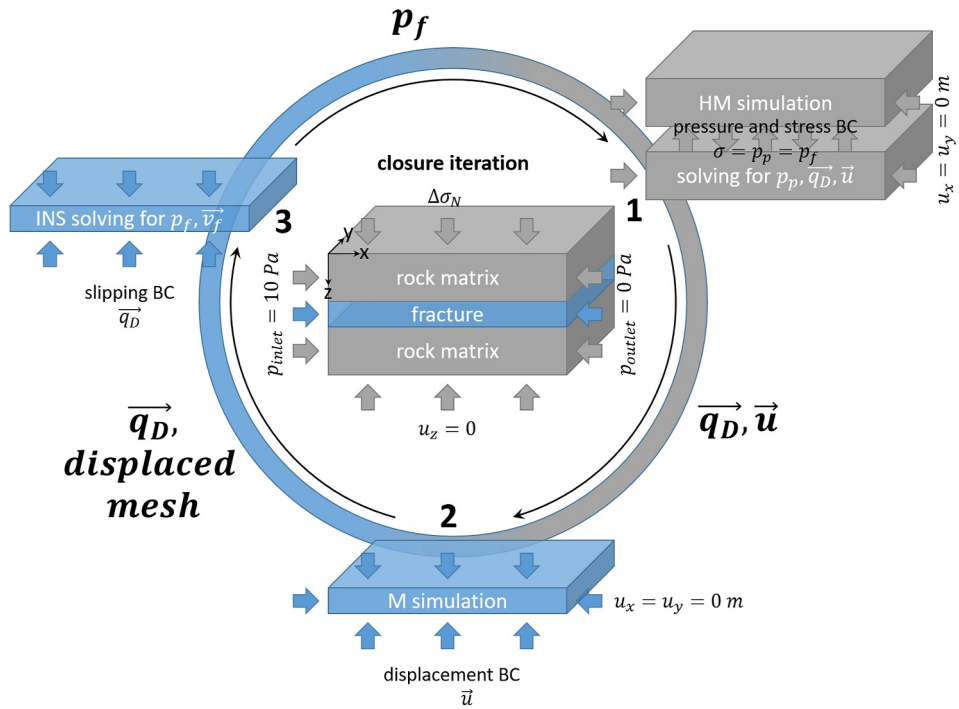

Figure 7. Workflow at each step of the fracture closure. At the center, the general feature of the model (for clarity of the figure, the roughness of the fracture boundaries is not represented and the open space of the fracture is sketched as a parallelepipedic volume). Starting from computation 1 (upper right): hydromechanical (HM) simulation in the rock matrix domain based on Equations 2–4 and the inherited boundary conditions; computation 2 (lower center): Mechanical (M) simulation to get the new shape of the fracture aperture using the kinematic model of fracture closure described in Section 2.3; computation 3 (upper left): Incompressible Navier-Stokes (INS) simulation in the open space of the fracture. For the next fracture closure, the same loop starts again.

simulations is given in Figure 7. The Navier-Stokes module solves Equation 5 for the fluid pressure and the displacement vector field inside the fracture domain (Blöcher et al., 2019). For the matrix domain, the primary variables are the pore pressure and the solid displacements. The fluid velocity in the porous matrix and the strain and stress fields are derived from these primary quantities via the poro-elastic coupling described in Equations 2 and 3. To derive a coupling between the two physical systems, that is, the open fracture and the rock domain, we define four exchange functions (i.e., FEM Boundary Conditions) along the interfaces between the rock and the fracture (Figure 8). Since the fluid pressure inside the fracture occurs almost instantaneously when compared to the time scale of pore pressure diffusion in the rock, we use this pressure as a boundary condition to solve for the pore pressure in the rock matrix system (Figure 8a). Furthermore, this pressure acts as an additional body force on the rock matrix following Equation 3. Therefore, we use the pressure as a boundary condition for the pressure equation (Equation 2). The impact of it on the resulting solid displacement is implicit via Equation 3 (see Figure 8a). We solve Equation 2 to obtain the pore pressure distribution inside the porous matrix and then compute (via Equation 4) the resultant Darcy flux, which we then convert in Darcy velocity to impose it as a slipping boundary condition for INS (Figure 7). The Darcy velocity is then assigned as a slipping boundary for the fracture flow inside the fault (Figure 8b). To impose the mechanical coupling and the corresponding deformation of the fault open space where fluid is circulating, the displacement values obtained from the kinematic model of the fracture closure (Section 2.3) are used to deform the mesh of the fracture domain (M simulation in Figure 7) and to compute the dynamic pressure and fluid velocity fields (INS simulation in Figure 7) (Blöcher et al., 2019).

To derive a closed-form solution for the fluid flow in the fracture-rock system and measure its permeability, we apply the following initial and boundary conditions (Figure 8). The initial condition for the rock matrix is a zero displacement field and zero pore pressure. Furthermore, the fluid pressure and the velocity inside the fracture are also set to zero. In addition to the boundary conditions applied at the fault-matrix interface, we impose a flow either in the *x*- or *y*-direction by setting a small inlet overpressure of 10 Pa either along the *x*- or *y*-direction, respectively, to avoid high Reynolds number solutions (see Figure 13). At the outlet, we keep the pressure

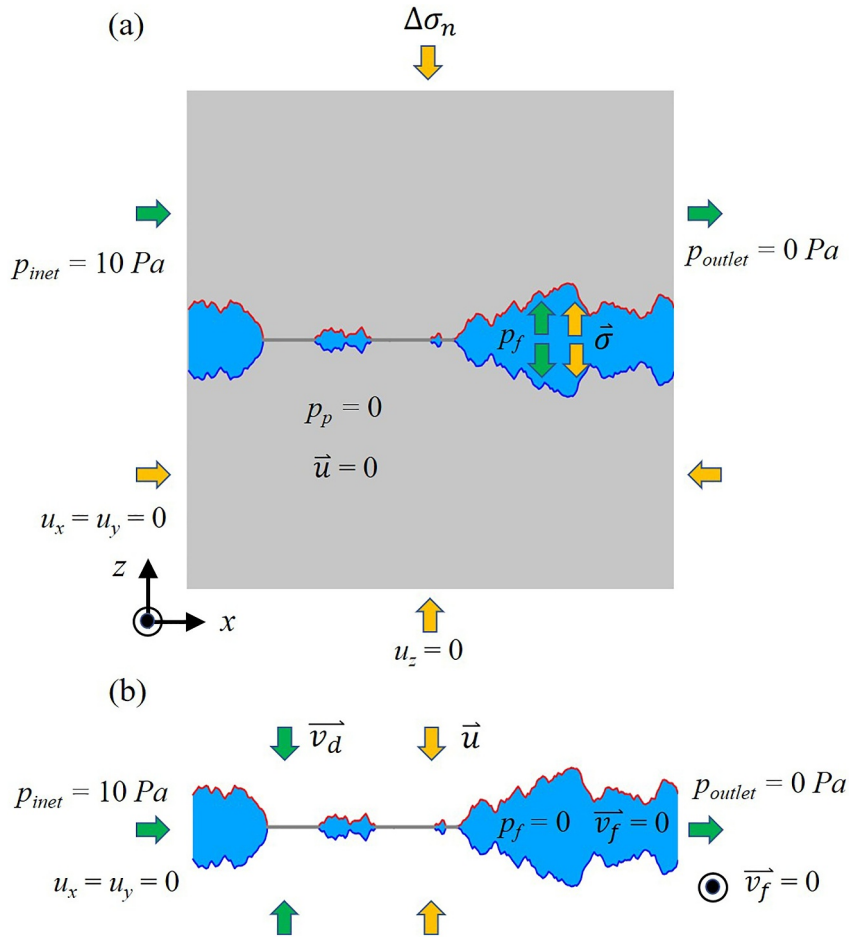

Figure 8. Cross-section view of the initial conditions and boundary conditions for (a) the rock matrix and (b) the fracture. Transfer functions at the fracture-rock interface are also illustrated.

constant at zero during the total transient simulation. For the mechanical part, we set a zero displacement in the *z*-direction for the bottom and no displacement in the *x*- and *y*-directions for the lateral borders, as well as for the inlet and outlet. At the top of the block, we apply normal loading to force deformation of the rock matrix, leading to consequent mechanical closure of the fracture. All material properties used in the modeling are listed in Table 1. We considered isotropic matrix permeability in this study, thus the permeability tensor is a scalar in the following. These values are representative of the well-known EGS project Soultz-sous-Forêts (Vallier et al., 2019).

2.5. Mesh Generation

The open fracture space is used as a 3D domain for finite element mesh generation. The domain is based on a regular grid along the mean plane of the fracture with a grid spacing of 1 m and dimensions of 256 m by 256 m (Figure 9a). The aperture ranges from a minimum of 0 m (i.e., contact areas) to a maximum of ~0.5 m (i.e., at zero closure).

The magnitude of the fracture opening is on the order of 0.1 m (Figure 2b), a characteristic value for fractures at the studied scale (~256 m) (Candela et al., 2012). The challenge for meshing such a geometry is to account for the extreme aspect ratio of the fracture volume, which can be as high as 1:1,000, making its meshing by isotropic voxels or elements particularly difficult for a similar resolution in the *z*-direction compared to the *x*- and *y*- directions. To represent a fracture opening with such an aspect ratio, we instead implement prism elements within an anisotropic mesh (Figure 9b). Normal to the fracture mean plane (i.e., along the *z*-direction), we use a discretization of the fracture open space by 8 layers of prism elements, with an aspect ratio of 1:25. The minimum

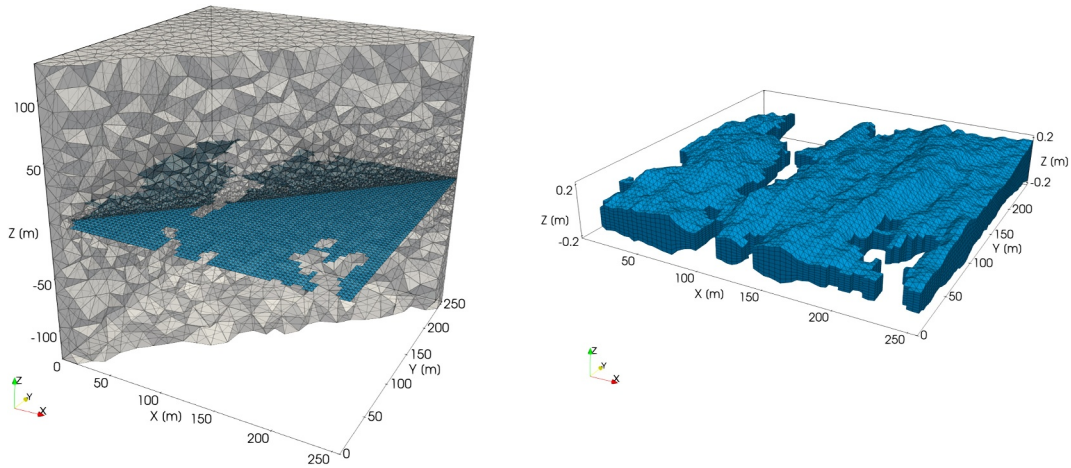

Figure 9. (left) Finite elements of the fracture open space (blue prisms) and of the rock matrix (gray tetraeders). Coarse-graining of the elements develops when moving away from the fracture. (right) Details of the meshing of the fracture open space (100-fold exaggerated in z-direction to emphasize the aperture fluctuations along the fracture).

element sizes normal and parallel to the fracture are 0.0125 and 1 m, respectively. For meshing the solid part, we use an isotropic tetrahedral mesh with an element size of $\sim$0.1 m close to the fracture, while the element size coarsens gradually with increasing distance from the fracture (Figure 9a). Meshing is performed by Gmsh (Geuzaine & Remacle, 2009), an open-source finite element mesh generator. For the open fracture space, we generate between 262,080 and 71,152 prism elements according to the closure degree of the fracture. For the solid part, we generate between 1,563,350 and 2,620,330 tetrahedral elements.

We use the flood-fill algorithm (Nosal, 2008) to determine the flow percolation threshold of a fault, that is, the state where the fracture flow loses connection between the inflow and outflow borders. If no flow path is found, the fault is marked as having reached/exceeded the percolation threshold.

3. Fracture Stiffness Evolution During Closure

The normal elastic response of a fracture is often quantified by the fracture normal stiffness κ (Goodman et al., 1968; L. Pyrak-Nolte & Morris, 2000; Morris et al., 2017; Jaeger et al., 2009; P. Lang et al., 2015):

$$\kappa = \frac{d\sigma_n}{du_f} \tag{6}$$

where σ_n is the applied normal stress and u_f is the associated displacement of the fracture, considered a deformable body (Figure 4). Equation 6 depicts the rigidity of the fracture as stress changes due to the closure of the fracture and the induced changes in the contact areas along the fracture.

3.1. Stress-Linear Stiffness Approach

Fracture stiffness measurements have been obtained using a variety of methods, such as laboratory experiments (Bandis et al., 1983; Cook, 1992; Kluge et al., 2020; Schrauf & Evans, 1986; Sun et al., 1985; Zhao & Brown, 1992), field tests (Jung, 1989; Pratt et al., 1977; Rutqvist et al., 1998), and numerical simulations (L. Pyrak-Nolte & Morris, 2000; L. Wang & Cardenas, 2016; Morris et al., 2017; Lavrov, 2017). Most studies measure a nonlinear increase in normal stress as a function of ongoing closure due to a linear increase in the stiffness from the applied stress, at least during the initial loading of the fracture (Cook, 1992). Such a process has also been shown to be irreversible when cyclic loading is applied (Kluge et al., 2020). In fact (Berthoud & Baumberger, 1998), directly showed this linear behavior of the fracture stiffness, as follows:

$$\kappa = \frac{\sigma_n}{l_0} \tag{7}$$

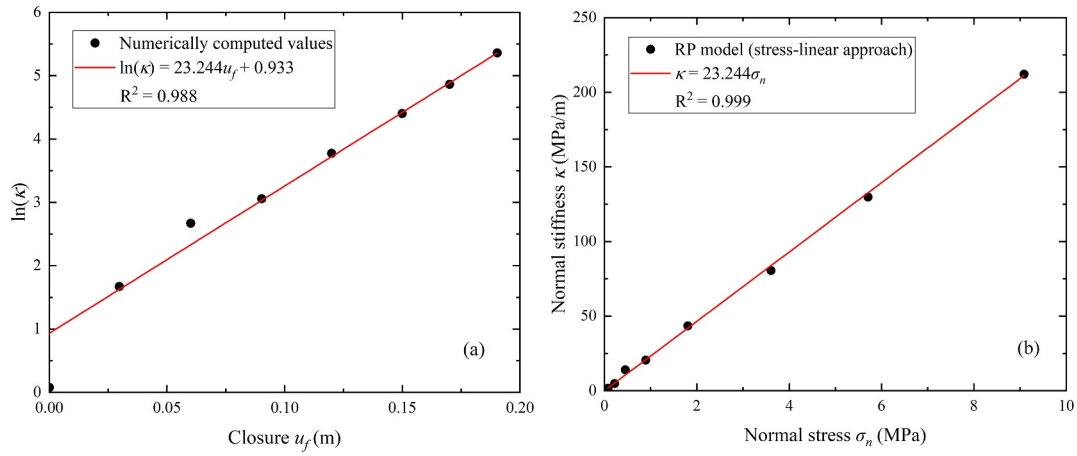

Figure 10. (a) Fitting of the fracture normal stiffness K as a function of fracture closure during the mechanical stage for F1 using the stress-linear stiffness approach. (b) Linear regression of the stiffness-stress data of the stress-linear stiffness approach.

where l_0 is a characteristic length related to the roughness of the surface. As proposed by Cook (1992), this linear property of the stiffness (Equation 7) together with its definition (Equation 6) lead to a simple differential equation (Pastewka et al., 2013), as follows:

$$\frac{d\sigma_n}{du_f} = \frac{\sigma_n}{l_0} \tag{8}$$

which has a solution in the form of a semi-logarithmic behavior of the stress, as classically observed in the following equation (Zangerl et al., 2008):

$$\ln(\sigma_n) = \chi \cdot \ u_f + \ln\left(\sigma_n^{ref}\right) \tag{9}$$

if one introduces the characteristic stiffness $\chi = 1/l_0$ and σ_n^{ref} as the reference normal stress, which refers to the effective normal stress level at the beginning of the test when $u_b = 0$, and is generally a small quantity (Goodman et al., 1968). The characteristic stiffness χ denotes the slope of the log-stress against the closure curve and defines the rate of change of normal stiffness and normal stress (Evans et al., 1992).

From Equation 7 and Equation 9, the behavior of the stiffness $\kappa\left(u_f\right)$ can be predicted as follows:

$$\ln(\kappa) = \chi \cdot u_f + \ln\left(\chi \cdot \sigma_n^{ref}\right) \tag{10}$$

In our model, to compute the fracture stiffness for a given closure u_f, we apply a small stress perturbation ($\Delta\sigma_n = 1$ MPa) along the top of the model and compute the corresponding volume change of the fracture ΔV_f. Dividing the volume change ΔV_f by the apparent fracture area A provides an estimate of the induced closure change $\Delta u_f = \Delta V_f / A$. The fracture stiffness κ at each closure step u_f can then be estimated as $\kappa = \Delta\sigma_n / \Delta u_f$. Figure 10a shows the evolution of the computed stiffness during closure for fault F1 (see Figure S3 in Supporting Information S1 for the other fault configurations). It demonstrates that the stiffness evolution modeled by our closure simulation is consistent with the largely observed Equation 10 (see e.g. Table 1 of Zangerl et al. (2008)). This semi-log behavior of our model validates the approximations made: on the one hand, the stress-linear stiffness approach - Equation 7 as illustrated in Figure 10b; on the other hand, the yield-contact area approach described in the next subsection. Equation 10 is then used to fit the evolution of the stiffness during closure and to obtain the stiffness characteristic: χ. Once the stiffness and the stiffness characteristic are known, we obtain the normal stress by means of Equation 7.

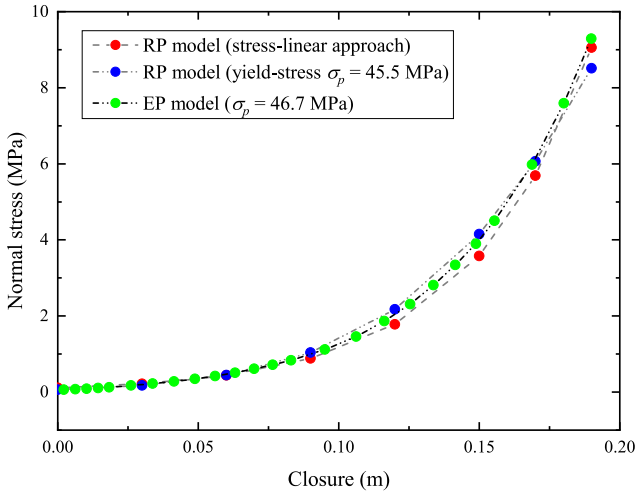

Figure 11. Comparison of different approaches to obtain the normal stress against fracture closure during the mechanical closure phase for fault F1: the red curve indicates the stress-linear method in the Bandis model; the blue curve indicates the elastic-limit method; and the green curve indicates the elasto-plastic (EP) model using the solution from the boundary element method as in Röttger et al. (2022) (see Supporting Information S1 Figures S3–S5).

The stiffness characteristic χ for fault F1 is estimated as $\chi = 23.2\text{m}^{-1}$ ($= 0.0232\text{mm}^{-1}$), which is a small value compared to the measured values (10–70 mm^{-1}) at the laboratory scale (Zangerl et al., 2008). For the other five faults, we obtain similar stiffness characteristic values of 18.7 m^{-1}, 23.2 m^{-1}, 23.0 m^{-1}, 24.6 m^{-1} and 27.6 m^{-1} (see Figure S3 in Supporting Information S1). Previous studies (e.g. (Pastewka et al., 2013),) have shown that the reciprocal of the stiffness characteristic $1/\chi$ (the characteristic length l_0) is of the order of the RMS roughness (h_{rms}) of the surfaces for nonadhesive solid contact surfaces. In our study, we obtain stiffness characteristics in the range of 18–27 m^{-1} for the 6 faults, indicating a characteristic length in the range of 0.04–0.05 m, which is consistent with the RMS of the fault surface (i.e., $h_{rms} = 0.045$ m).

3.2. A Yield-Contact Area Approach During Closure

We estimate the evolution of the absolute normal stress σ_n during closure using an independent approach based on the assumption that contact areas act as yield regions. Because the ratio of the applied normal stress and the normal stress along the fault asperities $\left(\sigma_n/\sigma_n^{asperities}\right)$ is equal to the ratio of the apparent area to the actual contact area (A/A_c), the stress concentration along the asperities (i.e., along contact areas) can be accessed. For example, with a 20% contact area, the applied stress is magnified by a factor of five at the asperities. Subsequently, with an applied stress of a few tens of MPa, the asperities might reach their elastic limits and enter the plastic domain. Following the "overlap" model approximation, we assume that the stress on all asperities is homogeneous when reaching the yield stress of the material σ_p:

$$\sigma_n^{asperities} \approx \sigma_p \tag{11}$$

Therefore, the applied normal stress can be approximated as follows:

$$\sigma_n \approx \sigma_p \cdot \frac{A_c}{A} \tag{12}$$

Considering the relationship between the contact area and fracture closure shown in Figure 6 and assuming that all asperities are at a stress level close to their compressive strength, the applied normal stress can be written as a function of the fracture closure as follows:

$$\sigma_n \approx \sigma_p \cdot \left(1 + erf\left(\left(u_f - \bar{h}\right)/\left(\sqrt{2}\,h_{rms}\right)\right)\right)/2 \tag{13}$$

The behavior of the applied normal stress with closure is then compared to that from the stress-linear approximation (Equation 9). Figure 11 presents the corresponding curves for both approaches. It is found that the best effective yield stress value is 45.5 MPa for fault F1 (similar values are obtained for other faults, as shown in Supporting Information S1, Figure S4). This effective yield stress is relatively low compared with the common elastic limit of rock (typically lower than the uniaxial compression strength (UCS)). However, it is consistent with the order of UCS if the scale effects of rock strength are considered (Thuro et al., 2001; Zhang et al., 2011). Indeed, according to the relationship between UCS and specimen size $UCS/UCS_{c50} = (50/d)^{0.18}$ proposed by Hoek and Brown (1980), where UCS_{c50} is the UCS of a 50-mm diameter specimen and d the diameter, we can estimate $UCS \approx 43$ MPa for our model (d is approximated by the block dimension) if we assume UCS_{c50} is on the order of 200 MPa. Here, UCS and d are in units of MPa and mm, respectively.

The good agreement between the two models illustrates that the normal stiffness during mechanical closure might be simply predicted from a single parameter, that is, yield stress σ_p, and the evolution of the contact area during closure (Figure 6). Interestingly, it also provides a physical origin of the semi-log behavior of the fracture stiffness

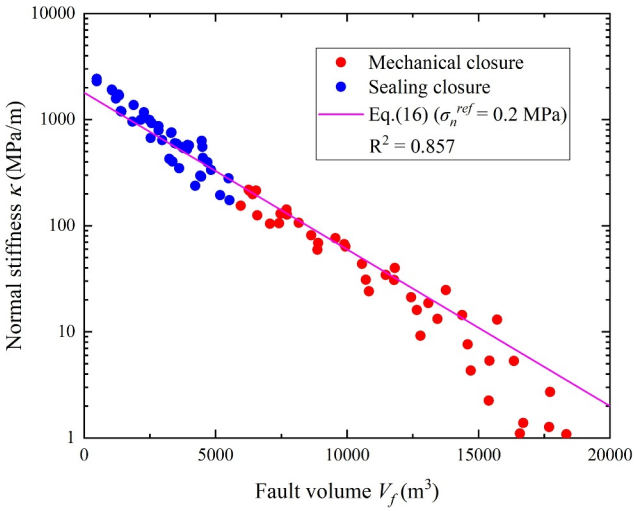

Figure 12. Log-linear plot of the fracture normal stiffness against the fault volume. Dots refer to the numerical simulations using the six synthetic faults used in this study. The pink line corresponds to the theoretical prediction from our rigid-plastic closure model of a self-affine fracture: Equation 15: $\kappa \approx \kappa_0 \exp(-V_f/V_f^c)$.

with closure and of the stiffness characteristics: the self-affine property of the fracture topography. In the in Supporting Information S1 (Figures S5a and S5b), we also check the linear behavior of the stiffness-stress curve obtained from the linear-stress approach and the yield-contact area approach, showing $\chi = 23.2\text{m}^{-1}$ and $\chi = 23.1\text{m}^{-1}$, respectively. To complete this check, we compute the stiffness-stress curve considering elasto-plastic rheology based on a boundary element method (BEM) (Röttger et al., 2022). We use a yield stress $\sigma_p = 46.7$ MPa, which provides a very similar evolution of the normal stress as a function of the fracture closure (Figure 11) and a linear relationship between stiffness and stress (see Figure S5c in Supporting Information S1). This, in turn, validates our stress-linear approximation.

3.3. Normal Fracture Stiffness and Fault Volume

The overall evolution of normal stress against fracture closure is shown in Figure 5. The normal stress increases with fracture closure during mechanical closure (pink zone), while it remains unchanged during sealing (cyan zone). The numerically computed normal stiffness is plotted as the slope at each closure u_f (red lines in Figure 5).

Since fracture closure u_f is not easily and directly accessible in the field, we propose in Figure 12 to describe the closure state of the fault in a different way. Specifically, we consider the open space volume of the fault V_f, which might be accessible through an injection test of the fault. Figure 6 shows that the fault closure varies between $(-3h_{rms}; 3h_{rms})$, where h_{rms} is the RMS of the fracture surface topography under free boundary conditions, that is, before any normal loading. In Figure S7 in Supporting Information S1, we show that the fault volume is well approximated by $V_f \approx A \cdot \left(6h_{rms} - u_f\right)$, where A is the apparent area of the fracture. Therefore, the fault closure can be written as follows:

$$u_f \approx 6h_{rms} - V_f/A \tag{14}$$

Substituting Equation 14 into Equation 10 and using $\chi = 1/h_{rms}$ yields the following:

$$\kappa \approx \kappa_0 \exp\left(-V_f/V_f^c\right) \tag{15}$$

with $\kappa_0 = e^6 \cdot \sigma_n^{ref}/h_{rms}$, the stiffness at full closure of the fault $\left(V_f = 0\right)$, and $V_f^c = A \cdot h_{rms}$ a characteristic volume of the fault. The reference normal stress σ_n^{ref} obtained here is approximately 0.2 MPa.

The evolution of the normal stiffness as a function of the open fault volume for the 6 synthetically generated faults, plotted in a log-lin space in Figure 12, shows that the predicted results (pink curve, Equation 15) are a good proxy of the numerical results (dots). This additionally verified the validity of the linear-stress approach to estimate the normal stress.

4. Fracture Permeability

4.1. Permeability Measurement

The effective fracture permeability is computed at the end of the workflow described in Figure 7 using the outputs of the computation, as an effective measurement of the hydraulic feature of the model for a given closure and using a parallel plate approximation as classically done for hydraulic aperture measurement (Blöcher et al., 2019). The permeability k of the overall system can then be determined after the steady state as follows:

$$k = -\frac{\mu_f L \dot{V}}{A_{side}\left(p_f^{in} - p_f^{out}\right)} \tag{16}$$

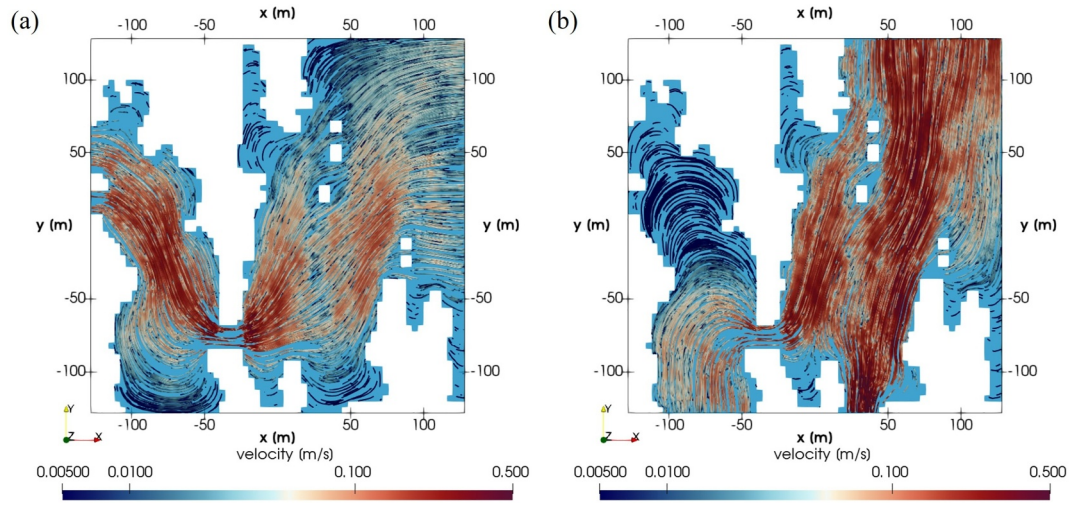

Figure 13. Map view of the flow inside fault F1. (a) Pressure drop is applied along the *x*-direction. (b) Pressure drop is applied along the *y*-direction. The white zones indicate the contact regions.

where L is the length of the block and $\dot{V}$ is the total fluid flux of the block obtained as the mean of the inlet flux $\dot{V}_{in}$ and outlet flux $\dot{V}_{out}$, that is, $\dot{V} = (\dot{V}_{in} + \dot{V}_{out})/2$, since they are almost identical (Equation 5). $\dot{V}_{in}$ and $\dot{V}_{out}$ can be computed as the sum of the inlet flux and the outlet flux of the fracture and the rock matrix, respectively: $\dot{V}_{in} = v_f^{in} A_f^{in} + v_m^{in} A_m^{in}$ and $\dot{V}_{out} = v_f^{out} A_f^{out} + v_m^{out} A_m^{out}$, where v_f and v_m are the fluid velocities of the fracture and matrix, and A_f and A_m are the areas of the fracture and matrix. The subscripts *in* and *out* indicate the inlet and outlet of the corresponding object (fracture or matrix), respectively. Since the model imposes the same pressure boundary conditions for the rock matrix and the fracture, the pressure at the inlet and the outlet of the block are constant over the whole related face of the model. Furthermore, there is almost no change in the total area of the block side A_{side} during the entire simulation.

The permeability is assessed by applying a small pressure gradient of 10 Pa/256 m to the block and computing the resulting fluid flux across the fault. Due to the low permeability of the matrix, most of the flow takes place along the open space of the fracture between the contact areas. The distribution of the velocity field in the fault-rock system also indicates that the permeability is dominated by the flow along the fault. Due to the surface roughness and the spatially correlated aperture distribution, a strong channeling effect is observed (with a maximum velocity magnitude of 0.5 m/s at the given pressure gradient of 10 Pa/256 m) along the flow path of the fault (Figure 13). In contrast, the maximum velocity magnitude in the matrix is approximately 1×10^{-13} m/s. Because of the low flow velocities in the matrix, it takes almost 10 years for the pressure and velocity field in the rock domain to reach a steady state.

Table 1
Material Properties Used in the Numerical Simulations

Property	Symbol	Value	Unit
Young's modulus	E	$25.0 \cdot 10^9$	Pa
Poisson ratio	ν	0.25	-
Biot coefficient	α	1	-
Matrix permeability	$\boldsymbol{k_m}$	$2.0 \cdot 10^{-16}$	m^2
Porosity	ϕ	0.085	-
Solid bulk modulus	K_s	$4.15 \cdot 10^{10}$	Pa
Fluid modulus	K_f	$2.2 \cdot 10^9$	Pa
Fluid viscosity	μ_f	0.001	Pa·s
Solid density	ρ_s	2,500	kg/m^3
Fluid density	ρ_f	1,000	kg/m^3

In addition, we observe a significant permeability anisotropy (Figure 13). The permeability of fault F1 in the *x*-direction (perpendicular to the fault slip direction) is smaller than that in the *y*-direction (perpendicular to the fault slip direction) during closure, showing flow anisotropic behavior.

4.2. Permeability Evolution

For either the mechanical or mineral sealing process, we impose a closure of ~0.03 m per step, except when approaching the percolation threshold, extra steps are considered between these steps. In the Supporting Information S1, Figure S6 illustrates some selected steps of the progressive closure (denoted as c0–c11) as maps of the open fault space for F1, and Figure S8 in Supporting Information S1 shows the related permeability in the *x*- and *y*-directions against the fault volume at each step of closure for all six faults. In terms of orders of magnitude, the fluxes along the *x*-direction and *y*-direction for case c0

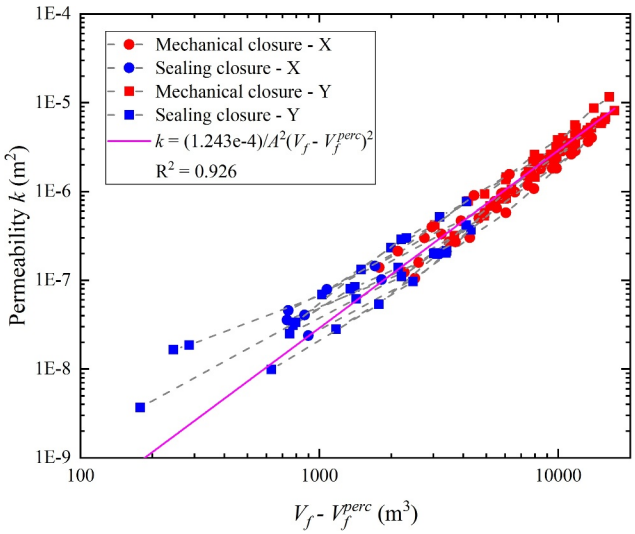

Figure 14. Evolution of the permeability k as a function of the percolation fault volume (the fault volume minus the fault volume at the percolation threshold $(V_f - V_f^{perc})$ for the 6 studied faults, which is fitted by $k \approx (B/A^2) \cdot (V_f - V_f^{perc})^2$, where A is the total block area and $B = 1.24 \times 10^{-4}$ is the geometrical prefactor.

(Figure S6a in Supporting Information S1) are 4.4 and 8.7 m^3/s, respectively. The computed permeability is in the range of $8 \times 10^{-7} m^2$. Due to progressive closure, the fault reaches the flow percolation threshold. For fault F1, the flow percolation threshold in the x-direction is between stages c5 (Figure 6f) and c6 (Figure S6g in Supporting Information S1). The transition of the fracture flow reduces the permeability of the overall system to $1.63 \times 10^{-15} m^2$, approximately 8 times the matrix permeability $2 \times 10^{-16} m^2$. By contrast, the permeability in the y-direction is only reduced from $3.77 \times 10^{-7} m^2$ (c0) to $2.3 \times 10^{-7} m^2$ (c6). The percolation threshold in the y-direction is between stages c8 (Figure S6i in Supporting Information S1) and c9 (Figure S6j in Supporting Information S1), which reduces the permeability from $3.16 \times 10^{-8} m^2$ to $5.26 \times 10^{-16} m^2$. The transition behavior of the permeability when reaching the flow percolation threshold is also observed for all other faults (Figures S8b–S8f in Supporting Information S1), with a similar magnitude reduction from $\sim 10^{-8} m^2$ to $\sim 10^{-15} m^2$.

In Figure 14, we compile all results in one figure by plotting the permeability against the percolated volume (i.e., the difference between the fault volume at the flow connection and at the percolation threshold). An overall quadratic evolution of the permeability above the percolation threshold is observed, as follows:

$$k \approx (B/A^2) \cdot \left(V_f - V_f^{perc}\right)^2 \tag{17}$$

which is an expected behavior from the linear relationship between the fault volume and the closure (Equation 14) assuming a proxy as a parallel plate model (i.e., a cubic law) where the permeability is related to the square of the fracture aperture, as follows: $h = V_f/A \approx \left(6h_{rms} - u_f\right)$.

4.3. Stiffness-Permeability Relationship

The permeability prediction is of key interest for subsurface reservoir engineering, such as enhanced geothermal systems, particularly when fluid circulation is dominated by a single fault. One way to predict the permeability is by fracture stiffness, which can be obtained by geophysical probing, for example, seismic wave measurements (L. J. Pyrak-Nolte et al., 1990; L. J. Pyrak-Nolte et al., 1992). This requires a quantitative relationship between permeability and stiffness. Several previous studies have been devoted to linking permeability and stiffness for lab-scale fractures under normal stress (L. Pyrak-Nolte & Morris, 2000; Petrovitch et al., 2013; L. Wang & Cardenas, 2016; Li et al., 2021). Here, based on the expressions established above for normal stiffness versus fault volume (Equation 15) and permeability versus fault volume (Equation 17), the stiffness and permeability can be related as follows:

$$\kappa = \kappa_0 \exp\left(-\left(A\sqrt{k/B} + V_f^{perc}\right)/V_f^c\right) \tag{18}$$

where V_f^{perc} at the percolation threshold might vary for different faults or in different directions. When we use a mean value of 3,000 m^3 (see Figure 16), it represents the numerical data well; see the pink curve in a log-lin plot (Figure 15) for stiffness against permeability.

Due to different roughness scaling properties in the two directions (i.e., $H_x = 0.8$ - perpendicular to slip and $H_y = 0.6$ - along slip direction), faults are generally more permeable along the y- direction. This is shown in Figure 15, as the data set in the y-direction (squares) lies essentially on top of the x-direction (dots).

4.4. Permeability Anisotropy at the Percolation Threshold

Close to the fluid flow percolation threshold, permeability significantly decreases and gradually approaches the matrix permeability (this transition is illustrated in Supporting Information S1 for each fracture, see Figure S8 in

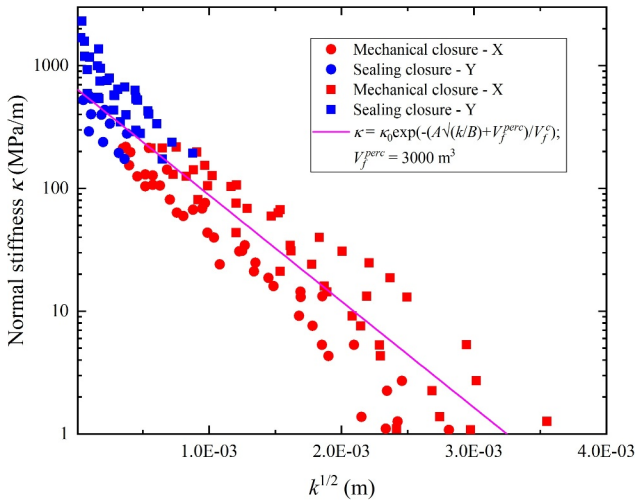

Figure 15. Fracture stiffness K as a function of the square root of permeability k. The pink line denotes the prediction from Equation 18 with a representative fault volume of 3,000 m^3 at the percolation threshold. Note that the evolution trend for flow along the Y-direction (squares), (i.e., shear direction), is typically with higher κ_0 than for flow in the X-direction (circles), (i.e., perpendicular to shear direction).

Supporting Information S1). For the large closure case (small volume), the permeability anisotropy is expected to be at a maximum, as the percolation threshold might be reached in one direction (at $V_f^{P_{max}}$) but not the other (at $V_f^{P_{min}}$), emphasizing the importance of permeability contrast.

We plot in a log-scale in Figure 16 the ratio of the permeability in the y-direction to the permeability in the x-direction as a function of the fault volume. When faults are below the percolation threshold in both directions because of a large closure (i.e., small fault volume below $V_f^{P_{min}}$) or above because of a low closure (i.e., large fault volume above $V_f^{P_{max}}$), the ratio k_y/k_x is close to one. When the permeability shows anisotropy, k_y/k_x jumps approximately seven orders of magnitude to $\sim 10^7$. This order is comparable to the ratio of the fracture permeability to the matrix permeability. We also observe that the emergence of the percolation threshold in the x-direction (at $V_f^{P_{max}}$) is not far from the transition from mechanical to sealing closure (transition from red to blue color in Figure 16). This shows that the preset transition from mechanical to chemical closure is in fact related to a strong change in the hydraulic fault properties. In addition, we show that fault volumes with large anisotropy (volumes between percolation thresholds $V_f^{P_{max}}$ and $V_f^{P_{min}}$) might cover different ranges, as illustrated by the behaviors of faults F1, F2 and F3, where the domain of high anisotropy is either reduced (F1), intermediate (F3) or large (F2). Note that F4 and F5 are similar to F3, and F6 is similar to F2; therefore, they are not shown here for better readability.

5. Discussion

5.1. Comparison With Laboratory and In-Situ Fracture Stiffness and Stiffness Characteristic Measurements

Previous studies have shown that fracture normal stiffness is related to a variety of factors, such as the elastic properties of the host rock, the distribution of the contact area, and the number of asperities (L. Pyrak-Nolte & Morris, 2000; Hopkins et al., 1987; Scholz, 2019). It is also essential to incorporate the fracture size when dealing with fracture normal stiffness. This is because rock samples measured in the lab are commonly of small size (~mm to ~cm), and therefore, there is a large difference in the fracture properties between the lab and the in-situ scale (~m to ~km). According to the power law scaling of the roughness amplitude for self-affine fracture surfaces (Candela et al., 2012), longer fractures typically have wider apertures and larger volumes and thereby become more compliant, as also revealed by previous studies (L. Pyrak-Nolte & Morris, 2000; Hobday & Worthington, 2012).

Figure 17 shows an experimental data set of fracture stiffness (blue dots) derived from a wide range of fracture length scales (Hobday & Worthington, 2012). For comparison, we present here the stiffness data from our numerical simulations at the 256 m scale with contact regions of ~20% (red squares) and ~60% (red stars), representing two degrees of fracture closure, that is, without any sealing at the end of the mechanical closure and with significant sealing, respectively. To illustrate the scale effect, we also conduct numerical modeling on several smaller fractures (i.e., 25.6 and 0.256 m) generated synthetically following the same power spectral density and RMS scaling as for the 256 m fractures (Figure 3). Although variations in the rock elastic properties are not considered, the overall numerical results of Figure 17 match well with the experimental data and show good consistency with the stiffness-dimension scaling relationship (dashed line) proposed by Worthington and Lubbe (2007).

The stiffness characteristic has been found to be rather constant for numerous fractures (Evans et al., 1992; Zangerl et al., 2008), from well-mated fractures in laboratory tests to reactivated hydrofractures in in-situ borehole tests. The values of the stiffness characteristic cover a broad range from 3 mm^{-1} to 720 mm^{-1} depending on the fracture area (blue and pink dots in Figure 18). In this study, we obtain the stiffness characteristic $\sim 100 \text{mm}^{-1}$ for an area of $6.55 \times 10^{-2} \text{m}^2$ (0.256 m scale), $\sim 0.2 \text{mm}^{-1}$ for an area of $6.55 \times 10^{2} \text{m}^2$ (25.6 m

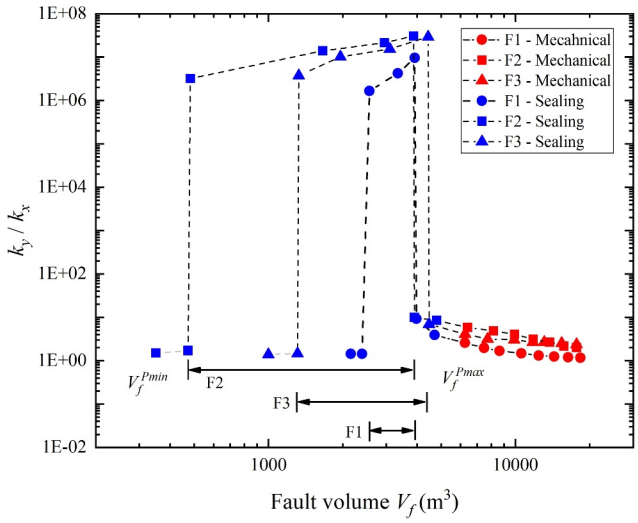

Figure 16. Evolution of the permeability ratio (k_y/k_x) as a function of the fault volume during the mechanical and sealing closure process for the three studied faults.

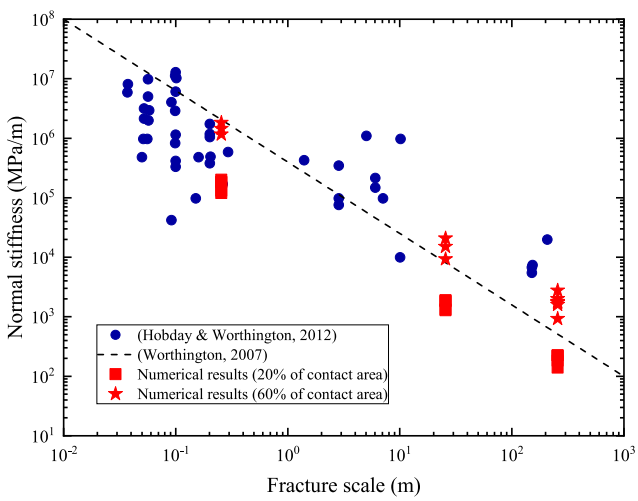

Figure 17. Scaling of fracture normal stiffness as a function of fracture length; modified from Hobday and Worthington (2012); Worthington and Lubbe (2007).

scale) and $\sim 0.02\text{mm}^{-1}$ for an area of $6.55 \times 10^4\text{m}^2$ (256 m scale), as shown by the red squares in Figure 18. Although Zangerl et al. (2008) concluded that there is only weak evidence of systematic scale effects for fracture cross-sectional areas larger than 100 cm^2, we obtain obvious scale effects and small variations in the stiffness characteristics of all studied faults at a given scale. This in turn suggests that under certain stress conditions, the prediction of normal stiffness is possible for such faults with self-affinity.

5.2. Implications for Reservoir Stimulation

In this study, we divide fracture closures into mechanical and sealing processes and simulate the coupled fluid flow and mechanical response during closure. Compared to previous studies that dealt with permeability and stiffness separately (Petrovitch et al., 2013; L. Wang & Cardenas, 2016; Li et al., 2021), our model allows access to both permeability and stiffness simultaneously. Moreover, we consider fluid exchange between the matrix and the fracture, the latter being a more realistic situation in practice compared to other models that generally ignore the matrix effect (Méheust & Schmittbuhl, 2000; L. Pyrak-Nolte & Morris, 2000; L. Wang & Cardenas, 2016). Although this effect seems to be negligible here when the matrix permeability is relatively low, the topic might be of great interest in future study.

In our model, we searched for stationary fluid flow and neglected possible fluid pressure diffusion, assuming that the time scale for fracture deformation was much larger than that of fluid pressure diffusion. This approximation can be discussed in the light of the work of Deng et al. (2021) who assessed the hydraulic diffusivity of a partially open fracture with similar features. They showed that the fracture hydraulic diffusivity of such a large fracture could be of the order of $10^2\text{m}^2/\text{s}$ close to the percolation threshold where the hydraulic aperture a_h is of the order of 10^{-4} m, with a fluid viscosity of 10^{-3} Pa·s and a fluid compressibility $\beta_f = 2.2$ GPa. With these parameters, the characteristic time for pressure diffusion along the fracture would be of the order of 10 min. Any increase of the aperture would reduce quadratically this characteristic time. The time scale to be compared is the deformation of the fracture. Any deformation that changes the hydraulic aperture at a time scale shorter than 10 min, will compete with the fluid pressure diffusion. An evaluation of the associated characteristic strain rate can be obtained from the magnitude of the hydraulic aperture $a_h = 10^{-4}$m of this large fracture, its characteristic thickness of the order of 0.3 m and the time scale of 10 min: $\dot{\epsilon} = 5 \cdot 10^{-7}\ s^{-1}$. In this sense, seismic processes or fast fluid injection might interfere but slow geological creep deformation will not.

The fracture sealing due to mineral precipitation is assumed to be time-independent and the precipitation growth rate is therefore constant everywhere. However, due to the channeling effect, the fluid velocity along the fracture will be different. This would affect the location of mineral precipitation and change the permeability (Ortoleva et al., 1987; Sausse, 2002; Wetzel et al., 2020). Time-dependent sealing may result in completely sealed fractures or partially sealed fractures at the same scale (Griffiths et al., 2016), that is, the mineral growth might be inhomogeneous in the fracture space. Moreover, previous studies on the alteration of fracture permeability by coupled mechanical and chemical processes have shown that contact regions can dissolve faster than the open fracture space under high flow rate conditions (e.g., Ameli et al. (2014)). The inhomogeneous precipitation/dissolution would modify the percolation threshold of the fracture flow in both directions compared to the homogeneous precipitation/dissolution. This would require the development of a coupled H-M-C model. Despite these assumptions and given the low flow rate assumed, the main conclusions derived in this study remain valid.

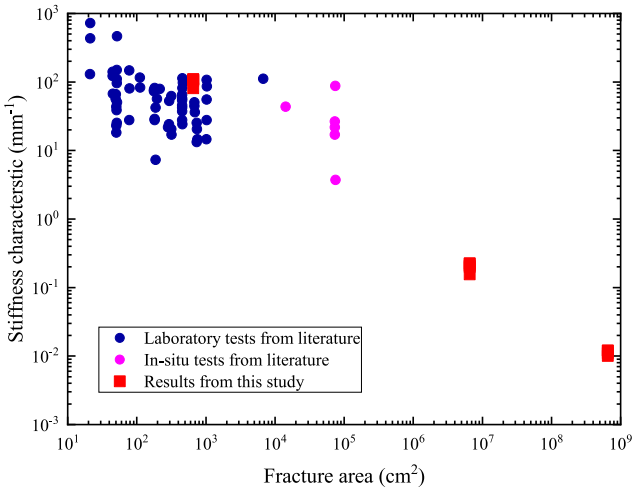

Figure 18. Fracture stiffness characteristic as a function of fracture area; modified from Zangerl et al. (2008).

In addition, we only consider mineral precipitation inside the fracture. Previous studies have shown that it might also occur in the pores (Griffiths et al., 2016). This may modify the permeability of the rock matrix and therefore the fluid exchange between the fracture and the matrix. However, the bulk effect would primarily lower the effective permeability of the matrix, so our conclusions, which are based on the assumption that the fracture flow dominates over the bulk matrix flow, will remain unaltered. In this case, the pore filling may have a limited influence on the whole permeability.

Other factors, such as temperature, may directly affect the mineral growth rate during the sealing process (Griffiths et al., 2016). Accounting for these additional effects requires a fully coupled T-H-M-C model, which will be considered in our future studies.

Finally, we can identify several implications in terms of permeability anisotropy during chemical stimulation of fractured reservoirs. First, from Figure 15, we see that the κ_0 stiffness is typically higher when flow is along the shear slip direction (y-direction). Second, if the fracture volume is larger than the percolation volume $V_f^{p_{\max}}$, that is, the fluid channels are connected in both directions, a chemical treatment might provide only a limited improvement in permeability. Third, if the fracture volume is lower than the percolation volume $V_f^{p_{\min}}$ or if it is between the percolation volume $V_f^{p_{\max}}$ and $V_f^{p_{\min}}$, that is, the fluid channels are fully sealed or only connected in one direction, a chemical treatment may significantly enhance the permeability in at least one direction. In the latter case, one should also consider the thickness of the minerals that needs to be dissolved to improve the permeability. It is neither economically nor technically available if too much chemical solvent is required. For example, according to Figure 16, if $V = 400$ m^3, we only need to dissolve a small layer of minerals ($\sim$0.01 m) for F2, but it requires three times or more for F1 and F6 to improve their permeability noticeably. In comparison, if $V = 4{,}000$ m^3, the chemical treatment might be available for all three fractures (the dissolved thickness <0.01 m). The fracture volume, which is directly related to the degree of sealing, might be used as a key parameter in the chemical treatment. Moreover, it can be determined once the normal stiffness is known because of their quantitative function relationship (Figure 12). The normal stiffness can in turn be derived relatively easily by field measurements. Therefore, through stiffness and permeability tests, it is possible to estimate the degree of sealing and evaluate a chemical treatment.

However, one should also note that if a critical stiffness is exceeded during the chemical treatment, that is, the lowest stiffness to maintain fault stability, faults are likely to close. Here, the critical state is defined as the transition from the mechanical to the sealing regime at 20% of the contact area (see Figure 16). When close to the transition zone, chemical stimulation should be avoided since fault collapse may in turn reduce the permeability. This critical state requires further evaluation for faults in a given environment. In summary, the degree of sealing, anisotropic flow behavior and critical stiffness are the key factors in the chemical stimulation of reservoir connectivity dominated by a single fault.

6. Conclusion

By means of a fully 3-dimensional finite element approach (MOOSE/GOLEM), we simulated the hydro-mechanical behavior of a partly sealed rough fracture embedded in a granite reservoir. Here, open multi-scale fractures with a very small aspect ratio (i.e., thickness vs. extension) of 1:1,000 were handled. The progressive closure of the fracture was modeled in two successive phases. First, a mechanical closure following a rigid-plastic model of the asperities in contact was introduced to describe the yield contact area from the self-affine geometry of the fracture. The model has been benchmarked by comparison with two independent approaches: one based on a stress-linear stiffness approximation as broadly empirically observed through the assessment of the stiffness characteristic and one from an independent boundary element method to reproduce an elasto-plastic closure. Second, a sealing of the fault was simulated by adding a stepwise coating to the fault surfaces, which progressively reduces the fault aperture. We defined the switch from one phase to the other at approximately 20% of the contact area based on experimental observations. It appears from our computation that this limit also corresponds to a specific closure of the fracture (approximately the rms of the fracture aperture roughness h_{rms}) and to the flow

percolation threshold along the fault slip perpendicular direction. At the percolation threshold, there is a dramatic reduction in permeability by ~8 orders of magnitude with a strong anisotropy. We also showed that the evolution of the fracture stiffness during closure follows a generic exponential law with the fracture volume, including a characteristic volume that is related to features of the fracture geometry and stiffness characteristic classically measured during mechanical tests. Moreover, a stiffness-permeability relationship has been obtained with a slight anisotropy with flow direction: higher stiffness along the shear direction. Implications for reservoir stimulations are important. Indeed, our results suggest that chemical treatments for fault-rock systems should consider multiple factors, such as the directional percolation threshold, anisotropic permeability, and appropriate fracture stiffness. Meanwhile, this risk of fault collapsing by chemical stimulation has to be considered when approaching the mechanical-sealing transition state.

Conflict of Interest

The authors declare no conflicts of interest relevant to this study.

Data Availability Statement

The Matlab code "Synthetic2DFault" provided in Candela et al. (2009) was used to produce the fracture aperture data sets shown in Figure 2 and Figure S1 in Supporting Information S1. The software MOOSE/GOLEM used in this paper is available at https://zenodo.org/records/999401 (Jacquey & Cacace, 2017) and described in Cacace and Jacquey (2017). The software "contact.engineering" used in this paper for computing elasto-plastic contact problems on rough surfaces is available on-line at https://contact.engineering/ and described in Röttger et al. (2022).

Acknowledgments

This work was supported by the European Commission Horizon 2020 research and innovation program (DESTRESS) [Grant 691728], the China Postdoctoral Science Foundation Funded Project [Grant 2023M740385], and the China Scholarship Council [Grant 201808510128]. Special thanks to the free platform "contact.engineering" for computing elasto-plastic contact problems on rough surfaces and for fruitful discussions with Prof. Lars Pastewka and Mr. Antoine Sanner. This work was performed under the framework of the Laboratory of Excellence LABEX ANR-11-LABX-0050-G-EAU-THERMIE-PROFONDE and the Interdisciplinary Thematic Institute GeoT, as part of the ITI 2021–2028 program of the University of Strasbourg, CNRS and Inserm, supported by IdEx Unistra (ANR 10 IDEX 0002) and by SFRI STRAT'US project (ANR 20 SFRI 0012) under the framework of the French Investments for the Future Program.

References

Adler, P. M., & Thovert, J.-F. (1999). *Fractures and fracture networks* (Vol. 15). Springer Science and Business Media. https://doi.org/10.1007/978-94-017-1599-7

Almqvist, A., Campana, C., Prodanov, N., & Persson, B. (2011). Interfacial separation between elastic solids with randomly rough surfaces: Comparison between theory and numerical techniques. *Journal of the Mechanics and Physics of Solids*, *59*(11), 2355–2369. https://doi.org/10.1016/j.jmps.2011.08.004

Ameli, P., Elkhoury, J. E., Morris, J. P., & Detwiler, R. L. (2014). Fracture permeability alteration due to chemical and mechanical processes: A coupled high-resolution model. *Rock Mechanics and Rock Engineering*, *47*(5), 1563–1573. https://doi.org/10.1007/s00603-014-0575-z

Bandis, S., Lumsden, A., & Barton, N. (1983). Fundamentals of rock joint deformation. *International Journal of Rock Mechanics and Mining Sciences and Geomechanics Abstracts*, *20*(6), 249–268. https://doi.org/10.1016/0148-9062(83)90595-8

Barton, N., & Choubey, V. (1977). The shear strength of rock joints in theory and practice. *Rock Mechanics*, *10*(1–2), 1–54. https://doi.org/10.1007/BF01261801

Batrouni, G. G., Hansen, A., & Schmittbuhl, J. (2002). Elastic response of rough surfaces in partial contact. *EPL*, *60*(5), 724–730. https://doi.org/10.1209/epl/i2002-00368-1

Berkowitz, B. (2002). Characterizing flow and transport in fractured geological media: A review. *Advances in Water Resources*, *25*(8–12), 861–884. https://doi.org/10.1016/S0309-1708(02)00042-8

Berthoud, P., & Baumberger, T. (1998). Shear stiffness of a solid–solid multicontact interface. *Proceedings of the Royal Society of London. Series A: Mathematical, Physical and Engineering Sciences*, *454*(1974), 1615–1634. https://doi.org/10.1098/rspa.1998.0223

Blöcher, G., Kluge, C., Milsch, H., Cacace, M., Jacquey, A. B., & Schmittbuhl, J. (2019). Permeability of matrix-fracture systems under mechanical loading–constraints from laboratory experiments and 3-d numerical modelling. *Advances in Geosciences*, *49*, 95–104. https://doi.org/10.5194/adgeo-49-95-2019

Bons, P. D., Elburg, M. A., & Gomez-Rivas, E. (2012). A review of the formation of tectonic veins and their microstructures. *Journal of Structural Geology*, *43*, 33–62. https://doi.org/10.1016/j.jsg.2012.07.005

Borri-Brunetto, M., Carpinteri, A., & Chiaia, B. (1999). Scaling phenomena due to fractal contact in concrete and rock fractures. In *Fracture scaling* (pp. 221–238). Springer. https://doi.org/10.1007/978-94-011-4659-3_12

Bouchaud, E. (1997). Scaling properties of cracks. *Journal of Physics: Condensed Matter*, *9*(21), 4319–4344. https://doi.org/10.1088/0953-8984/9/21/002

Brodsky, E. E., Gilchrist, J. J., Sagy, A., & Collettini, C. (2011). Faults smooth gradually as a function of slip. *Earth and Planetary Science Letters*, *302*(1–2), 185–193. https://doi.org/10.1016/j.epsl.2010.12.010

Brown, S. R., & Scholz, C. H. (1985). Broad bandwidth study of the topography of natural rock surfaces. *Journal of Geophysical Research*, *90*(B14), 12575–12582. https://doi.org/10.1029/JB090iB14p12575

Cacace, M., & Jacquey, A. B. (2017). Flexible parallel implicit modelling of coupled thermal–hydraulic–mechanical processes in fractured rocks. *Solid Earth*, *8*(5), 921–941. https://doi.org/10.5194/se-8-921-2017

Caine, J. S., Evans, J. P., & Forster, C. B. (1996). Fault zone architecture and permeability structure. *Geology*, *24*(11), 1025–1028. https://doi.org/10.1130/0091-7613(1996)024⟨1025:FZAAPS⟩2.3.CO;2

Candela, T., Renard, F., Bouchon, M., Brouste, A., Marsan, D., Schmittbuhl, J., & Voisin, C. (2009). Characterization of fault roughness at various scales: Implications of three-dimensional high resolution topography measurements. *Pure and Applied Geophysics*, *166*(10–11), 1817–1851. https://doi.org/10.1007/s00024-009-0521-2

Candela, T., Renard, F., Klinger, Y., Mair, K., Schmittbuhl, J., & Brodsky, E. E. (2012). Roughness of fault surfaces over nine decades of length scales. *Journal of Geophysical Research*, *117*(B8), B08409. https://doi.org/10.1029/2011JB009041

Carbone, G., & Bottiglione, F. (2008). Asperity contact theories: Do they predict linearity between contact area and load? *Journal of the Mechanics and Physics of Solids*, *56*(8), 2555–2572. https://doi.org/10.1016/j.jmps.2008.03.011
Cook, N. G. (1992). Natural joints in rock: Mechanical, hydraulic and seismic behaviour and properties under normal stress. *International Journal of Rock Mechanics and Mining Sciences & Geomechanics Abstracts*, *29*(3), 198–223. https://doi.org/10.1016/0148-9062(92)93656-5
Cornet, F. H. (2015). *Elements of crustal geomechanics*. Cambridge University Press. https://doi.org/10.1017/CBO9781139034050
Cox, S. F. (2005). Coupling between deformation, fluid pressures, and fluid flow in ore-producing hydrothermal systems at depth in the crust. *Economic Geology*, *100*, 39–75. https://doi.org/10.5382/AV100.04
Dapp, W. B., Lücke, A., Persson, B. N., & Müser, M. H. (2012). Self-affine elastic contacts: Percolation and leakage. *Physical Review Letters*, *108*(24), 244301. https://doi.org/10.1103/PhysRevLett.108.244301
Davis, G. H., Reynolds, S. J., & Kluth, C. F. (2011). *Structural geology of rocks and regions*. John Wiley and Sons.
De Dreuzy, J.-R., Méheust, Y., & Pichot, G. (2012). Influence of fracture scale heterogeneity on the flow properties of three-dimensional discrete fracture networks (DFN). *Journal of Geophysical Research*, *117*(B11). https://doi.org/10.1029/2012JB009461
Deng, Q., Blöcher, G., Cacace, M., & Schmittbuhl, J. (2021). Hydraulic diffusivity of a partially open rough fracture. *Rock Mechanics and Rock Engineering*, *54*(10), 1–23. https://doi.org/10.1007/s00603-021-02629-2
Durney, D. (1973). Incremental strains measured by syntectonic crystal growths. *Gravity and Tectonics*, 67–96.
Elkhoury, J. E., Ameli, P., & Detwiler, R. L. (2013). Dissolution and deformation in fractured carbonates caused by flow of CO_2-rich brine under reservoir conditions. *International Journal of Greenhouse Gas Control*, *16*, S203–S215. https://doi.org/10.1016/j.ijggc.2013.02.023
Evans, K., Kohl, T., Rybach, L., & Hopkirk, R. (1992). *The effects of fracture normal compliance on the long term circulation behavior of a hot dry rock reservoir: A parameter study using the new fully-coupled code "fracture"* (Vol. 16, pp. 449–456). Geothermal Resources Council.
Fardin, N., Stephansson, O., & Jing, L. (2001). The scale dependence of rock joint surface roughness. *International Journal of Rock Mechanics and Mining Sciences*, *38*(5), 659–669. https://doi.org/10.1016/S1365-1609(01)00028-4
Geuzaine, C., & Remacle, J.-F. (2009). Gmsh: A 3-d finite element mesh generator with built-in pre-and post-processing facilities. *International Journal for Numerical Methods in Engineering*, *79*(11), 1309–1331. https://doi.org/10.1002/nme.2579
Goodman, R. E., Taylor, R. L., & Brekke, T. L. (1968). A model for the mechanics of jointed rock. *Journal of the Soil Mechanics and Foundations Division*, *94*(3), 637–659. https://doi.org/10.1061/JSFEAQ.0001133
Griffiths, L., Heap, M., Wang, F., Daval, D., Gilg, H., Baud, P., et al. (2016). Geothermal implications for fracture-filling hydrothermal precipitation. *Geothermics*, *64*, 235–245. https://doi.org/10.1016/j.geothermics.2016.06.006
Gudmundsson, A. (2011). *Rock fractures in geological processes*. Cambridge University Press. https://doi.org/10.1017/CBO9780511975684
Hansen, A., Schmittbuhl, J., Batrouni, G. G., & de Oliveira, F. A. (2000). Normal stress distribution of rough surfaces in contact. *Geophysical Research Letters*, *27*(22), 3639–3642. https://doi.org/10.1029/2000GL011757
Hobday, C., & Worthington, M. (2012). Field measurements of normal and shear fracture compliance. *Geophysical Prospecting*, *60*(3), 488–499. https://doi.org/10.1111/j.1365-2478.2011.01000.x
Hoek, E., & Brown, E. (1980). *Underground excavations in rock. Institution of mining and metallurgy*. Chapman and Hall. https://doi.org/10.1201/9781482288926
Hopkins, D. L., Cook, N. G., & Myer, L. R. (1987). Fracture stiffness and aperture as a function of applied stress and contact geometry. In *The 28th us symposium on rock mechanics (USRMS)*.
Huang, N., Liu, R., Jiang, Y., Cheng, Y., & Li, B. (2019). Shear-flow coupling characteristics of a three-dimensional discrete fracture network-fault model considering stress-induced aperture variations. *Journal of Hydrology*, *571*, 416–424. https://doi.org/10.1016/j.jhydrol.2019.01.068
Huenges, E., & Ledru, P. (2011). *Geothermal energy systems: Exploration, development, and utilization*. John Wiley and Sons. https://doi.org/10.1002/9783527630479
Hyun, S., Pei, L., Molinari, J.-F., & Robbins, M. O. (2004). Finite-element analysis of contact between elastic self-affine surfaces. *Physical Review E*, *70*(2), 026117. https://doi.org/10.1103/PhysRevE.70.026117
Ishibashi, T., Watanabe, N., Hirano, N., Okamoto, A., & Tsuchiya, N. (2015). Beyond-laboratory-scale prediction for channeling flows through subsurface rock fractures with heterogeneous aperture distributions revealed by laboratory evaluation. *Journal of Geophysical Research: Solid Earth*, *120*(1), 106–124. https://doi.org/10.1002/2014JB011555
Jacobs, T. D., Junge, T., & Pastewka, L. (2017). Quantitative characterization of surface topography using spectral analysis. *Surface Topography: Metrology and Properties*, *5*(1), 013001. https://doi.org/10.1088/2051-672X/aa51f8
Jacquey, A. B., & Cacace, M. (2017). Golem, a moose-based application [Software]. *Zenedo*. https://doi.org/10.5281/zenodo.999400
Jacquey, A. B., Cacace, M., & Blöcher, G. (2017). Modelling coupled fluid flow and heat transfer in fractured reservoirs: Description of a 3d benchmark numerical case. *Energy Procedia*, *125*, 612–621. https://doi.org/10.1016/j.egypro.2017.08.227
Jaeger, J. C., Cook, N. G., & Zimmerman, R. (2009). *Fundamentals of rock mechanics*. John Wiley and Sons. https://doi.org/10.1007/978-3-7091-2834-3
Jung, R. (1989). Hydraulic in situ investigations of an artificial fracture in the Falkenberg granite. *International Journal of Rock Mechanics and Mining Sciences and Geomechanics Abstracts*, *26*(3–4), 301–308. https://doi.org/10.1016/0148-9062(89)91978-5
Kim, I., Lindquist, W., & Durham, W. (2003). Fracture flow simulation using a finite-difference lattice Boltzmann method. *Physical Review E*, *67*(4), 046708. https://doi.org/10.1103/PhysRevE.67.046708
Kluge, C., Blöcher, G., Barnhoorn, A., & Bruhn, D. (2020). Hydraulic-mechanical properties of microfaults in granitic rock using the punch-through shear test. *International Journal of Rock Mechanics and Mining Sciences*, *134*, 104393. https://doi.org/10.1016/j.ijrmms.2020.104393
Kluge, C., Blöcher, G., Barnhoorn, A., Schmittbuhl, J., & Bruhn, D. (2021a). Permeability evolution during shear zone initiation in low-porosity rocks. *Rock Mechanics and Rock Engineering*, *54*(10), 1–24. https://doi.org/10.1007/s00603-020-02356-0
Kluge, C., Bruhn, D., Schmittbuhl, J., Hofmann, H., Blöcher, G., & Barnhoorn, A. (2021b). The stress-memory effect of fracture stiffness during cyclic loading in low permeability sandstone. *Journal of Geophysical Research: Solid Earth*, *126*(10), e2020JB021469. https://doi.org/10.1029/2020JB021469
Kluge, C., Milsch, H., & Blöcher, G. (2017). Permeability of displaced fractures. *Energy Procedia*, *125*, 88–97. https://doi.org/10.1016/j.egypro.2017.08.077
Lang, P., Paluszny, A., & Zimmerman, R. (2015). Hydraulic sealing due to pressure solution contact zone growth in siliciclastic rock fractures. *Journal of Geophysical Research: Solid Earth*, *120*(6), 4080–4101. https://doi.org/10.1002/2015JB011968
Lang, P. S., Paluszny, A., Nejati, M., & Zimmerman, R. W. (2018). Relationship between the orientation of maximum permeability and intermediate principal stress in fractured rocks. *Water Resources Research*, *54*(11), 8734–8755. https://doi.org/10.1029/2018wr023189
Lang, P. S., Paluszny, A., & Zimmerman, R. W. (2016). Evolution of fracture normal stiffness due to pressure dissolution and precipitation. *International Journal of Rock Mechanics and Mining Sciences*, *88*, 12–22. https://doi.org/10.1016/j.ijrmms.2016.06.004

Laubach, S. E. (2003). Practical approaches to identifying sealed and open fractures. *AAPG Bulletin*, *87*(4), 561–579. https://doi.org/10.1306/11060201106

Lavrov, A. (2017). Fracture permeability under normal stress: A fully computational approach. *Journal of Petroleum Exploration and Production Technology*, *7*(1), 181–194. https://doi.org/10.1007/s13202-016-0254-6

Li, B., Cui, X., Zou, L., & Cvetkovic, V. (2021). On the relationship between normal stiffness and permeability of rock fractures. *Geophysical Research Letters*, *48*(20), e2021GL095593. https://doi.org/10.1029/2021gl095593

Liu, J., Sheng, J., Polak, A., Elsworth, D., Yasuhara, H., & Grader, A. (2006). A fully-coupled hydrological–mechanical–chemical model for fracture sealing and preferential opening. *International Journal of Rock Mechanics and Mining Sciences*, *43*(1), 23–36. https://doi.org/10.1016/j.ijrmms.2005.04.012

Matsuki, K., Chida, Y., Sakaguchi, K., & Glover, P. (2006). Size effect on aperture and permeability of a fracture as estimated in large synthetic fractures. *International Journal of Rock Mechanics and Mining Sciences*, *43*(5), 726–755. https://doi.org/10.1016/j.ijrmms.2005.12.001

Meakin, P. (1998). *Fractals, scaling and growth far from equilibrium* (Vol. 5). Cambridge University Press. https://doi.org/10.5555/2018799

Méheust, Y., & Schmittbuhl, J. (2000). Flow enhancement of a rough fracture. *Geophysical Research Letters*, *27*(18), 2989–2992. https://doi.org/10.1029/1999GL008464

Méheust, Y., & Schmittbuhl, J. (2001). Geometrical heterogeneities and permeability anisotropy of rough fractures. *Journal of Geophysical Research*, *106*(B2), 2089–2102. https://doi.org/10.1029/2000JB900306

Méheust, Y., & Schmittbuhl, J. (2003). Scale effects related to flow in rough fractures. *Pure and Applied Geophysics*, *160*(5), 1023–1050. https://doi.org/10.1007/PL00012559

Morris, J. P., Jocker, J., & Prioul, R. (2017). Numerical investigation of alternative fracture stiffness measures and their respective scaling behaviours. *Geophysical Prospecting*, *65*(3), 791–807. https://doi.org/10.1111/1365-2478.12441

Mourzenko, V. V., Thovert, J.-F., & Adler, P. M. (1995). Permeability of a single fracture; validity of the Reynolds equation. *Journal de Physique: II*, *5*(3), 465–482. https://doi.org/10.1051/jp2:1995133

Neuville, A., Toussaint, R., & Schmittbuhl, J. (2010a). Fracture roughness and thermal exchange: A case study at Soultz-Sous-Forêts. *Comptes Rendus Geoscience*, *342*(7–8), 616–625. https://doi.org/10.1016/j.crte.2009.03.006

Neuville, A., Toussaint, R., & Schmittbuhl, J. (2010b). Hydrothermal coupling in a self-affine rough fracture. *Physical Review E*, *82*(3), 036317. https://doi.org/10.1103/PhysRevE.82.036317

Noiriel, C., Gouze, P., & Made, B. (2013). 3d analysis of geometry and flow changes in a limestone fracture during dissolution. *Journal of Hydrology*, *486*, 211–223. https://doi.org/10.1016/j.jhydrol.2013.01.035

Nosal, E.-M. (2008). Flood-fill algorithms used for passive acoustic detection and tracking. In *2008 new trends for environmental monitoring using passive systems* (pp. 1–5). https://doi.org/10.1109/PASSIVE.2008.4786975

Okamoto, A., & Sekine, K. (2011). Textures of syntaxial quartz veins synthesized by hydrothermal experiments. *Journal of Structural Geology*, *33*(12), 1764–1775. https://doi.org/10.1016/j.jsg.2011.10.004

Ortoleva, P., Merino, E., Moore, C., & Chadam, J. (1987). Geochemical self-organization i; reaction-transport feedbacks and modeling approach. *American Journal of Science*, *287*(10), 979–1007. https://doi.org/10.2475/ajs.287.10.979

Parry, W. (1998). Fault-fluid compositions from fluid-inclusion observations and solubilities of fracture-sealing minerals. *Tectonophysics*, *290*(1–2), 1–26. https://doi.org/10.1016/S0040-1951(98)00013-4

Pastewka, L., Prodanov, N., Lorenz, B., Müser, M. H., Robbins, M. O., & Persson, B. N. (2013). Finite-size scaling in the interfacial stiffness of rough elastic contacts. *Physical Review E*, *87*(6), 062809. https://doi.org/10.1103/PhysRevE.87.062809

Pei, L., Hyun, S., Molinari, J., & Robbins, M. O. (2005). Finite element modeling of elasto-plastic contact between rough surfaces. *Journal of the Mechanics and Physics of Solids*, *53*(11), 2385–2409. https://doi.org/10.1016/j.jmps.2005.06.008

Persson, B. N. (2006). Contact mechanics for randomly rough surfaces. *Surface Science Reports*, *61*(4), 201–227. https://doi.org/10.1016/j.surfrep.2006.04.001

Persson, B. N., Albohr, O., Tartaglino, U., Volokitin, A., & Tosatti, E. (2004). On the nature of surface roughness with application to contact mechanics, sealing, rubber friction and adhesion. *Journal of Physics: Condensed Matter*, *17*(1), R1–R62. https://doi.org/10.1088/0953-8984/17/1/R01

Peterson, J. W., Lindsay, A. D., & Kong, F. (2018). Overview of the incompressible Navier–Stokes simulation capabilities in the moose framework. *Advances in Engineering Software*, *119*, 68–92. https://doi.org/10.1016/j.advengsoft.2018.02.004

Petrovitch, C. L., Nolte, D. D., & Pyrak-Nolte, L. J. (2013). Scaling of fluid flow versus fracture stiffness. *Geophysical Research Letters*, *40*(10), 2076–2080. https://doi.org/10.1002/grl.50479

Plouraboué, F., Kurowski, P., Hulin, J.-P., Roux, S., & Schmittbuhl, J. (1995). Aperture of rough cracks. *Physical Review E*, *51*(3), 1675–1685. https://doi.org/10.1103/PhysRevE.51.1675

Power, W. L., & Tullis, T. E. (1991). Euclidean and fractal models for the description of rock surface roughness. *Journal of Geophysical Research*, *96*(B1), 415–424. https://doi.org/10.1029/90JB02107

Pratt, H., Swolfs, H., Brace, W., Black, A., & Handin, J. (1977). Elastic and transport properties of an in situ jointed granite. *International Journal of Rock Mechanics and Mining Sciences & Geomechanics Abstracts*, *14*(1), 35–45. https://doi.org/10.1016/0148-9062(77)90560-5

Pyrak-Nolte, L., & Morris, J. (2000). Single fractures under normal stress: The relation between fracture specific stiffness and fluid flow. *International Journal of Rock Mechanics and Mining Sciences*, *37*(1–2), 245–262. https://doi.org/10.1016/S1365-1609(99)00104-5

Pyrak-Nolte, L. J. (2019). Fracture specific stiffness: The critical link between the scaling behavior of hydro-mechanical coupling in fractures and seismic monitoring. In *Science of carbon storage in deep saline formations* (pp. 311–335). Elsevier.

Pyrak-Nolte, L. J., Myer, L. R., & Cook, N. G. (1990). Transmission of seismic waves across single natural fractures. *Journal of Geophysical Research*, *95*(B6), 8617–8638. https://doi.org/10.1029/JB095iB06p08617

Pyrak-Nolte, L. J., Xu, J., & Haley, G. M. (1992). Elastic interface waves propagating in a fracture. *Physical Review Letters*, *68*(24), 3650–3653. https://doi.org/10.1103/PhysRevLett.68.3650

Ramsay, J. G. (1980). The crack–seal mechanism of rock deformation. *Nature*, *284*(5752), 135–139. https://doi.org/10.1038/284135a0

Renard, F., Voisin, C., Marsan, D., & Schmittbuhl, J. (2006). High resolution 3d laser scanner measurements of a strike-slip fault quantify its morphological anisotropy at all scales. *Geophysical Research Letters*, *33*(4). https://doi.org/10.1029/2005GL025038

Röttger, M. C., Sanner, A., Thimons, L. A., Junge, T., Gujrati, A., Monti, J. M., et al. (2022). Contact. engineering—Create, analyze and publish digital surface twins from topography measurements across many scales [Software]. *Surface Topography: Metrology and Properties*, *10*(3), 035032. https://doi.org/10.1088/2051-672x/ac860a

Rutqvist, J., Noorishad, J., Tsang, C.-F., & Stephansson, O. (1998). Determination of fracture storativity in hard rocks using high-pressure injection testing. *Water Resources Research*, *34*(10), 2551–2560. https://doi.org/10.1029/98WR01863

Sagy, A., Brodsky, E. E., & Axen, G. J. (2007). Evolution of fault-surface roughness with slip. *Geology*, *35*(3), 283–286. https://doi.org/10.1130/G23235A.1

Sahimi, M. (1993). Flow phenomena in rocks: From continuum models to fractals, percolation, cellular automata, and simulated annealing. *Reviews of Modern Physics*, *65*(4), 1393–1534. https://doi.org/10.1103/RevModPhys.65.1393

Sausse, J. (2002). Hydromechanical properties and alteration of natural fracture surfaces in the Soultz granite (Bas-Rhin, France). *Tectonophysics*, *348*(1–3), 169–185. https://doi.org/10.1016/S0040-1951(01)00255-4

Sayers, C. M., Taleghani, A. D., & Adachi, J. (2009). The effect of mineralization on the ratio of normal to tangential compliance of fractures. *Geophysical Prospecting*, *57*(3), 439–446. https://doi.org/10.1111/j.1365-2478.2008.00746.x

Schmittbuhl, J., Chambon, G., Hansen, A., & Bouchon, M. (2006). Are stress distributions along faults the signature of asperity squeeze? *Geophysical Research Letters*, *33*(13). https://doi.org/10.1029/2006GL025952

Schmittbuhl, J., Gentier, S., & Roux, S. (1993a). Field measurements of the roughness of fault surfaces. *Geophysical Research Letters*, *20*(8), 639–641. https://doi.org/10.1029/93GL00170

Schmittbuhl, J., Schmitt, F., & Scholz, C. (1995a). Scaling invariance of crack surfaces. *Journal of Geophysical Research*, *100*(B4), 5953–5973. https://doi.org/10.1029/94JB02885

Schmittbuhl, J., Vilotte, J.-P., & Roux, S. (1993b). Percolation through self-affine surfaces. *Journal of Physics A: Mathematical and General*, *26*(22), 6115–6133. https://doi.org/10.1088/0305-4470/26/22/014

Schmittbuhl, J., Vilotte, J.-P., & Roux, S. (1995b). Reliability of self-affine measurements. *Physical Review E*, *51*(1), 131–147. https://doi.org/10.1103/PhysRevE.51.131

Scholz, C. H. (2019). *The mechanics of earthquakes and faulting*. Cambridge University Press. https://doi.org/10.1017/9781316681473

Schrauf, T., & Evans, D. (1986). Laboratory studies of gas flow through a single natural fracture. *Water Resources Research*, *22*(7), 1038–1050. https://doi.org/10.1029/WR022i007p01038

Sun, Z., Gerrard, C., & Stephansson, O. (1985). Rock joint compliance tests for compression and shear loads. *International Journal of Rock Mechanics and Mining Sciences and Geomechanics Abstracts*, *22*(4), 197–213. https://doi.org/10.1016/0148-9062(85)92948-1

Thuro, K., Plinninger, R., Zäh, S., & Schütz, S. (2001). Scale effects in rock strength properties. Part 1: Unconfined compressive test and Brazilian test. In *Isrm regional symposium, Eurock* (pp. 169–174).

Tse, R., & Cruden, D. (1979). Estimating joint roughness coefficients. *International Journal of Rock Mechanics and Mining Sciences and Geomechanics Abstracts*, *16*(5), 303–307. https://doi.org/10.1016/0148-9062(79)90241-9

Vallet, C., Lasseux, D., Zahouani, H., & Sainsot, P. (2009). Sampling effect on contact and transport properties between fractal surfaces. *Tribology International*, *42*(8), 1132–1145. https://doi.org/10.1016/j.triboint.2009.02.013

Vallier, B., Magnenet, V., Schmittbuhl, J., & Fond, C. (2019). Large scale hydro-thermal circulation in the deep geothermal reservoir of Soultz-Sous-Forêts (France). *Geothermics*, *78*, 154–169. https://doi.org/10.1016/j.geothermics.2018.12.002

Walsh, R., McDermott, C., & Kolditz, O. (2008). Numerical modeling of stress-permeability coupling in rough fractures. *Hydrogeology Journal*, *16*(4), 613–627. https://doi.org/10.1007/s10040-007-0254-1

Wang, L., & Cardenas, M. B. (2016). Development of an empirical model relating permeability and specific stiffness for rough fractures from numerical deformation experiments. *Journal of Geophysical Research: Solid Earth*, *121*(7), 4977–4989. https://doi.org/10.1002/2016JB013004

Wang, M., Chen, Y.-F., Ma, G.-W., Zhou, J.-Q., & Zhou, C.-B. (2016). Influence of surface roughness on nonlinear flow behaviors in 3d self-affine rough fractures: Lattice Boltzmann simulations. *Advances in Water Resources*, *96*, 373–388. https://doi.org/10.1016/j.advwatres.2016.08.006

Wetzel, M., Kempka, T., & Kühn, M. (2020). Hydraulic and mechanical impacts of pore space alterations within a sandstone quantified by a flow velocity-dependent precipitation approach. *Materials*, *13*(14), 3100. https://doi.org/10.3390/ma13143100

Worthington, M., & Lubbe, R. (2007). The scaling of fracture compliance. *Geological Society, London, Special Publications*, *270*(1), 73–82. https://doi.org/10.1144/GSL.SP.2007.270.01.05

Zangerl, C., Evans, K., Eberhardt, E., & Löw, S. (2008). Normal stiffness of fractures in granitic rock: A compilation of laboratory and in-situ experiments. *International Journal of Rock Mechanics and Mining Sciences*, *45*(8), 1500–1507. https://doi.org/10.1016/j.ijrmms.2008.02.001

Zhang, Q., Zhu, H., Zhang, L., & Ding, X. (2011). Study of scale effect on intact rock strength using particle flow modeling. *International Journal of Rock Mechanics and Mining Sciences*, *48*(8), 1320–1328. https://doi.org/10.1016/j.ijrmms.2011.09.016

Zhao, J., & Brown, E. (1992). Hydro-thermo-mechanical properties of joints in the carnmenellis granite. *The Quarterly Journal of Engineering Geology and Hydrogeology*, *25*(4), 279–290. https://doi.org/10.1144/GSL.QJEG.1992.025.04.03

Zhou, J., Zhang, L., Qi, S., & Yang, D. (2020). Empirical ratio of dynamic to static stiffness for propped artificial fractures under variable normal stress. *Engineering Geology*, *273*, 105683. https://doi.org/10.1016/j.enggeo.2020.105683

Zimmerman, R., & Main, I. (2004). Hydromechanical behavior of fractured rocks. *International Geophysics Series*, *89*, 363–422. https://doi.org/10.1016/S0074-6142(03)80023-2

Zimmerman, R. W., & Bodvarsson, G. S. (1996). Hydraulic conductivity of rock fractures. *Transport in Porous Media*, *23*(1), 1–30. https://doi.org/10.1007/BF00145263